

Fractal-constrained deep learning for super-resolution of turbulence with zero or few label data



Jiaxin Wu ^{a,b}, Min Luo ^{a,*}, Boo Cheong Khoo ^b, Dunhui Xiao ^c, Pengzhi Lin ^d

^a Ocean College, Zhejiang University, Zhoushan 316021, Zhejiang, China

^b Department of Mechanical Engineering, National University of Singapore, 117575, Singapore

^c School of Mathematical Sciences, Key Laboratory of Intelligent Computing and Applications (Ministry of Education), Tongji University, Shanghai 200092, China

^d State Key Laboratory of Hydraulics and Mountain River Engineering, Sichuan University, Chengdu 610065, China

ARTICLE INFO

Keywords:

Flow reconstruction
Fractal theory
Turbulent flow
Energy cascade
Physics-informed deep learning

ABSTRACT

The super-resolution of turbulence is of paramount importance and still remains challenging due to the inefficiency of the current technologies in retaining the intrinsic physics like the multi-scale flow structures and energy cascades. To address this challenge, this work proposes a fractal-constrained deep learning super-resolution model termed SKFSR-FIC. The model is characterized by two distinctive designs: (1) a SKip-connected Feature-reuse Super-Resolution (SKFSR) network that learns and retains multi-scale flow structures and multi-frequency dynamics, achieving efficient upscaling of flow fields while reconstructing self-similar physics; (2) a fractal invariance constraint (FIC) that utilizes the self-similarities of flow properties invariant to scales to substitute label data information in super resolution, thus achieving accurate reconstruction of multi-scale dynamics and energy cascades. The SKFSR-FIC model, for the first time, leverages fractal dimensions to guide the turbulent flow reconstruction and significantly reduces the reliance on label data and, especially, achieves zero-shot (i.e., unsupervised) super-resolution that cannot be handled by existing deep learning models. The results from five self-affine fractal images and two turbulent flow cases demonstrate the enhanced efficiency (up to 2 times) and accuracy (up to 100 times) of the unsupervised SKFSR-FIC model compared to the conventional interpolation method and deep learning models. Moreover, the SKFSR network is compatible with both FIC and label data, thereby adaptively enabling unsupervised, supervised and semi-supervised learning strategies. In particular, the semi-supervised SKFSR-FIC model, even by using one snapshot, achieves the best accuracy among the three learning strategies due to the combination of physics and data.

1. Introduction

Turbulence is a complex fluid dynamic phenomenon characterized by multi-scale vortex interactions and the evolution of large-scale structures to small-scale ones [1,2]. Throughout the evolution of turbulence, fluid dynamic quantities (e.g., velocity, pressure and temperature) fluctuate across a broad range of frequencies, accompanying the spatial-temporal intermittent flow structures [3–5]. From the energy perspective, the kinetic energies intermixed within large-scale structures of turbulence nonlinearly transfer into those of small-scale flow structures, i.e., the direct energy cascade [6,7]. Resolving the complex dynamic behaviors and energy transfers of turbulence invariably requires data at very fine observation scales, i.e., high-resolution (HR) data [8,9]. The HR data can be obtained by different ways, like performing

fine-mesh numerical simulations that solve partial differential equations (PDEs) and conducting high-resolution experimental or field measurements by deploying many sensors. However, the solving for and storage/analysis of these HR or high-dimensional data are very costly or even infeasible [10,11].

Super-resolution (SR) is a crucial technique that can reconstruct HR turbulent flows from low-resolution (LR) ones [12,13]. In numerical simulations, finite-resolution simulations (e.g., RANS and LES) can be conducted by using affordable computational resources and based on the produced data, high resolution (e.g., DNS) data can be reconstructed by a SR technique [8,14–18]. In experiment studies, SR methods have been utilized to reconstruct global flow fields from sparse measurements, thereby enhancing experimental feasibility and reducing costs [15,19]. In general, traditional SR methods can be categorized into the

* Corresponding author.

E-mail address: min.luo@zju.edu.cn (M. Luo).

model-based and interpolation-based methods [13]. The former builds a numerical model that maps low-dimensional spatiotemporal data (represented as an information matrix) to high-dimensional outputs. However, the solving process of this kind of method may be ill-conditioned, which is time-consuming or even impossible to achieve converged results [20,21]. The interpolation method (e.g., cubic interpolation method), is more efficient and has been widely applied. However, this category of method may lead to non-negligible errors in obtaining local flow information through interpolation [22,23].

To overcome the limitations of traditional SR techniques in handling highly-nonlinear fluid dynamic problems, deep learning (DL) has been incorporated into SR modeling. The DL-based SR (call DLSR for short) models, particularly those based on supervised learning, utilize a labeled subset of data (hence are commonly termed data-driven methods) for iteratively optimizing model parameters during the offline training process [24]. Due to the augmented techniques adopted in network training, DL techniques offer superior capability of modeling, thereby addressing the inefficiency of traditional approaches related to ill-conditioned problems [21]. In the online stage after the training converges, DLSR models can conduct computations efficiently via pre-built nonlinear transformation functions from input data to HR labels [25]. The superior approximation capability and online efficiency make DLSR models widely applied in the SR reconstruction of experimental data [26–29] and numerical results [19,22,30,31] of periodical flows, jets, cardiovascular flows and ocean currents [24,32,33]. Additionally, the data mining capability of DL enables the capture of small-scale structures in turbulent flows, which cannot be handled by traditional interpolation methods. However, the accuracy of these data-driven methods significantly deteriorates when performing data extrapolation, i.e., handling data not covered by the training sets [34]. This poses difficulties in predicting turbulent flows, which manifests spatial-temporal nonlinear dynamics with multi-scale structures. Also, even with sufficient label data, the high-dimensional datasets adversely affect the convergence rate in training DLSR models, while only improve the model's accuracy marginally.

Unsupervised DLSR, which requires no HR label data for training, has been obtaining significant developments [35,36]. The Generative Adversarial Networks (GANs) are commonly employed in DLSR, often defined as unsupervised or semi-supervised (by using very few labels) learning models [21,37]. GANs generate HR flow fields with features closely resembling real data (labels) through adversarial training of two deep networks [22]. Various studies, including cylinder wake flows, isotropic turbulence, turbulent rotating flows and wall-bounded flows [14,38,39], have demonstrated the capability of GANs in HR flow reconstruction by using a small number of labels. Results demonstrate the viability of GANs in generating intermittent and small-scale flow structures although high computational costs are required for the aforementioned adversarial training strategy. Also, for the sake of computational efficiency, most GANs do not impose extra physical constraints and hence have the issue of pseudo-generation, i.e., large extrapolation errors [30,40,41]. Therefore, incorporating the intrinsic physics of fluid dynamics into DLSR models in an efficient manner is essential for further enhancing the accuracy, especially the extrapolation accuracy, of DLSR models [33,42].

Fractal refers to a geometric shape characterized by complex structures and interfaces that exhibit self-similarities across different scales, and turbulence is a prominent example manifesting fractal dynamics [43,44]. Fractal theory has been applied to analyze complex systems with irregular bifurcation patterns through evaluating the intrinsic self-similarity that can be quantified by the fractal dimension [45–47]. The self-similarity, also known as scale invariance, is independent on the observation scale (i.e., resolution) [48–50]. Specifically, during the dynamic evolution of turbulence, the self-similarity of fluid structures remains unchanged, implying that turbulent flows (or other complex fluid systems) are governed by invariant flow modes (i.e., attractors) [5, 51]. From the kinetic energy perspective, the spatial-temporal evolution

dominated by invariant attractors implies a self-similarity in the corresponding energy cascade [52,53]. Documented experimental and numerical results [54–56] suggest that turbulence structures across a wide range of scales exhibit similar energy dissipation characteristics, thereby demonstrating the self-similarity and scale independence of the turbulence kinetic energy (TKE). In particular, the energy spectra of high-frequency turbulent flows, especially those in the inertial subrange, exhibits a positive correlation to the fractal dimension [56,57]. Thus, leveraging scale-invariant self-similarity as *priori* is an essential for regularizing DL models, being similar to physics-informed neural networks (PINNs) that require defined governing equations to apply physical constraints [58]. Additionally, models incorporating the scale invariant does not require the solving of PDEs in applying the constraint and hence are computationally efficient. However, the key of implementing the fractal constraint in DL-based models is to compute the fractal dimension, the accuracy and efficiency of which are still challenging.

This study proposes a fractal invariance-constrained deep learning super resolution model called SKFSR-FIC for handling turbulence. For the first time, the scale invariance in the fractal theory is incorporated as physical priori, for enhancing the accuracy and efficiency in HR reconstruction of turbulent flows. SKFSR-FIC possesses twofold novelties: (1) a deep learning network SKFSR, designed for learning multi-scale intrinsic self-similar features that dominants turbulent flows, and; (2) the differentiable fractal invariance constraint (FIC), which incorporates self-similarity as the physical constraint to reconstruct multi-frequency and multi-scale flow fields and energy cascades. The features make SKFSR-FIC capable of zero-shot super-resolution that cannot be handled by traditional DL models, as sketched in Fig. 1.

2. Methodology

2.1. Concepts and key formulations of SKFSR

Suppose the LR input snapshot matrix is $\mathbf{x}^{\text{LR}} \in \mathbb{R}^{m \times n}$, which can be flow parameters like velocity, stress, vorticity, temperature, concentration, etc. [59]. Here, $m = L_a^{\text{LR}} L_\beta^{\text{LR}}$ represents the number of spatially-discretized grids along the horizontal and vertical axes in a two-dimensional space, and n denotes the number of discretized time steps. From the LR inputs, DLSR models output reconstructed HR snapshots $\hat{\mathbf{x}}^{\text{SR}}$ that approximate the true information \mathbf{x}^{HR} (i.e., the label), which can be described as

$$\mathbf{x}^{\text{HR}} = \underbrace{F(\mathbf{x}^{\text{LR}}; \mathbf{w})}_{\hat{\mathbf{x}}^{\text{SR}}} + e, \quad (1)$$

where F denotes the mapping function of DLSR model (e.g., the proposed SKFSR), \mathbf{w} represents the learnable weights of the model (i.e., hyperparameters). The HR-scale output is computed by $\hat{\mathbf{x}}^{\text{SR}} = F(\mathbf{x}^{\text{LR}}) \approx \mathbf{x}^{\text{HR}}$ as illustrated by the red solid line in Fig. 2 (a), where $\mathbf{x}^{\text{HR}}, \hat{\mathbf{x}}^{\text{SR}} \in \mathbb{R}^{M \times n}$ and $M = m f_u^2$. The upscaling factor $f_u \in \mathbb{N}^*$ is applied on each spatial axis, such that $M = L_a^{\text{SR}} L_\beta^{\text{SR}} = (f_u L_a^{\text{LR}}) \cdot (f_u L_\beta^{\text{LR}})$. The residual between $\hat{\mathbf{x}}^{\text{SR}} \in \mathbb{R}^{M \times n}$ and \mathbf{x}^{HR} is denoted as e . A commonly used objective function for evaluating DLSR model is the L_2 -norm error i.e., the mean squared error (MSE, denoted by L_{data}) between the SR-resolved snapshots and the true snapshots, with the best-fit weights defined as

$$\mathbf{w}_s = \underset{\mathbf{w}}{\operatorname{argmin}} \underbrace{\|\mathbf{x}^{\text{HR}} - F(\mathbf{x}^{\text{LR}}; \mathbf{w})\|_2^2}_{L_{\text{data}}}, \quad (2)$$

The proposed SKFSR model adopts convolutional layers as fundamental components for sampling feature maps (i.e., the input snapshots processed by SKFSR). Each convolution layer employs a weighted matrix K (corresponding to the primary hyperparameters) to perform the sliding-window convolution operation. The scale-invariance property

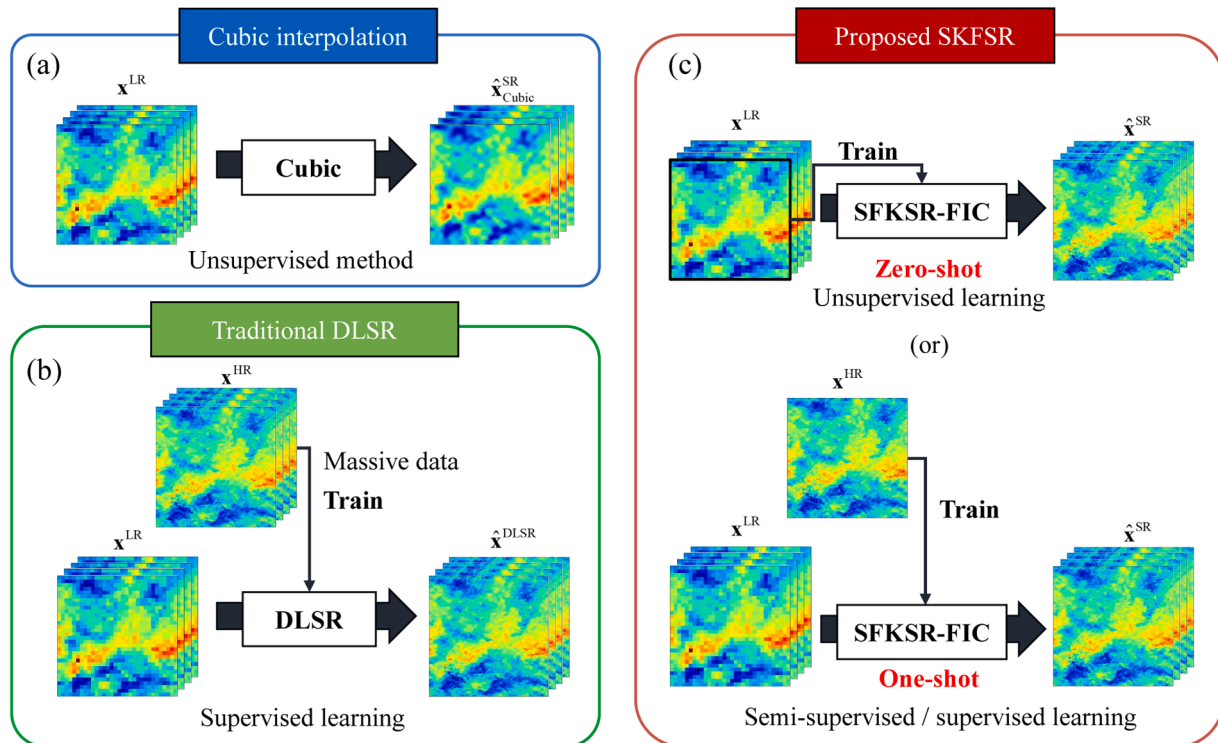


Fig. 1. Overview of super-resolution methods compared in this study: (a) traditional cubic spline interpolation requires no pre-training process nor HR labels; (b) traditional DLSR requires massive quantity of HR labels for achieving supervised learning that requires as few as one label.

and efficiency of the convolutional layers in extracting spatial features make SKFSR good at spatial super resolution of highly-nonlinear fluid flows that exhibit intrinsic flow patterns [60].

The SKFSR network architecture consists of three main parts, i.e., encoder, decoder and upscaler, as illustrated in Fig. 2 (b). The encoder consists of four down-sampling units, each is composed of a convolutional layer and a pooling layer. The down-sampling unit is designed to extract down-sampled spatial features at multi-scales. In the decoder, the low-dimensional feature maps undergo up-sampling through four deconvolutional units, increasing the spatial scale of the features to produce high-dimensional feature maps. Skip connections in encoder-decoder network enable the reuse of features at the same scale. Specifically, the encoded feature maps are concatenated with the corresponding dimensional feature maps in the decoder, as indicated by the dashed lines in Fig. 2 (b). The structure of feature reuse smooths the loss function hypersurface, thereby preventing the optimization from getting trapped in local minima, reducing the number of hyperparameters, and enhancing the efficiency of convergence to the optimal solution [61–63]. For SR tasks, the proposed model introduces cross-resolution feature reuse, as marked by the deep blue dashed lines in Fig. 2 (b). The encoded feature maps are up-sampled and then input to the decoder units that handle maps with upscaled resolution. This way strengthens the multi-scale self-similarity attention mechanism of the network. Then, the feature maps are fed into the upscaler, which consists of pixel shuffling (PS) and multi-resolution convolution (MRConv) layers. The upscaler convolves the feature maps by using multi-scale windows for obtaining feature maps of different scales, as well as outputs super-resolution snapshots with increased upscaling ratios. Trainable parameters of the proposed SKFSR network are detailed in Appendix A. Notably, the upscaler can be flexibly transferred to congeneric deep learning models for SR tasks.

The distinctive network design of SKFSR excels at perceiving the multi-scale self-similar features from a limited number of input data. As illustrated above, an essential step of boosting the SKFSR network lies in

the accurate and efficient computation and incorporation of the fractal dimension. To achieve this, a fractal invariance constraint (FIC) is proposed as elaborated in the following section.

2.2. Fractal invariance constraint

To enhance the capability of SKFSR model in perceiving and reconstructing multi-scale invariant flow structures, this study proposes an optimizable constraint incorporating the scale-invariance or the fractal dimension, which is termed the fractal invariance constraint (FIC). The FIC is assisted by proposing a differentiable box-counting (for computing fractal dimensions) algorithm, which addresses the issue of error back propagation existing in traditional approaches and hence helps in training the SKFSR model for better optimized parameters [46]. The FIC is also computationally efficient for two reasons. Firstly, it imposes the physical constraint via a statistical physical quantity, i.e. the fractal dimension, which avoids solving partial differential equations [64]. Secondly, the tensorized computation of FIC does not need the time-consuming executions, like the grid search and nest loops in conventional box-counting computations. The overall FIC computation flowchart is illustrated in Fig. 2 (a), where solid arrows represent the forward computation, and dashed arrows indicate the back propagation of errors. Note that the FIC is implemented by optimizing a weighted two-component loss function as

$$L_{\text{fractal}} = l_s + \lambda l_f, \quad (3)$$

where \$l_s\$ denotes the multi-scale spatial sampling loss, and \$l_f\$ is the fractal self-similarity loss. The weighting coefficient \$\lambda\$ in the loss function adjusts the contributions from the spatially coherent fluid structures (i.e., \$l_s\$) and the posterior indicators of self-similarity (i.e., \$l_f\$), which are elaborated in the following sections.

2.2.1. The multi-scale spatial sampling loss \$l_s\$

Among the two components, \$l_s\$ activates the network's attention

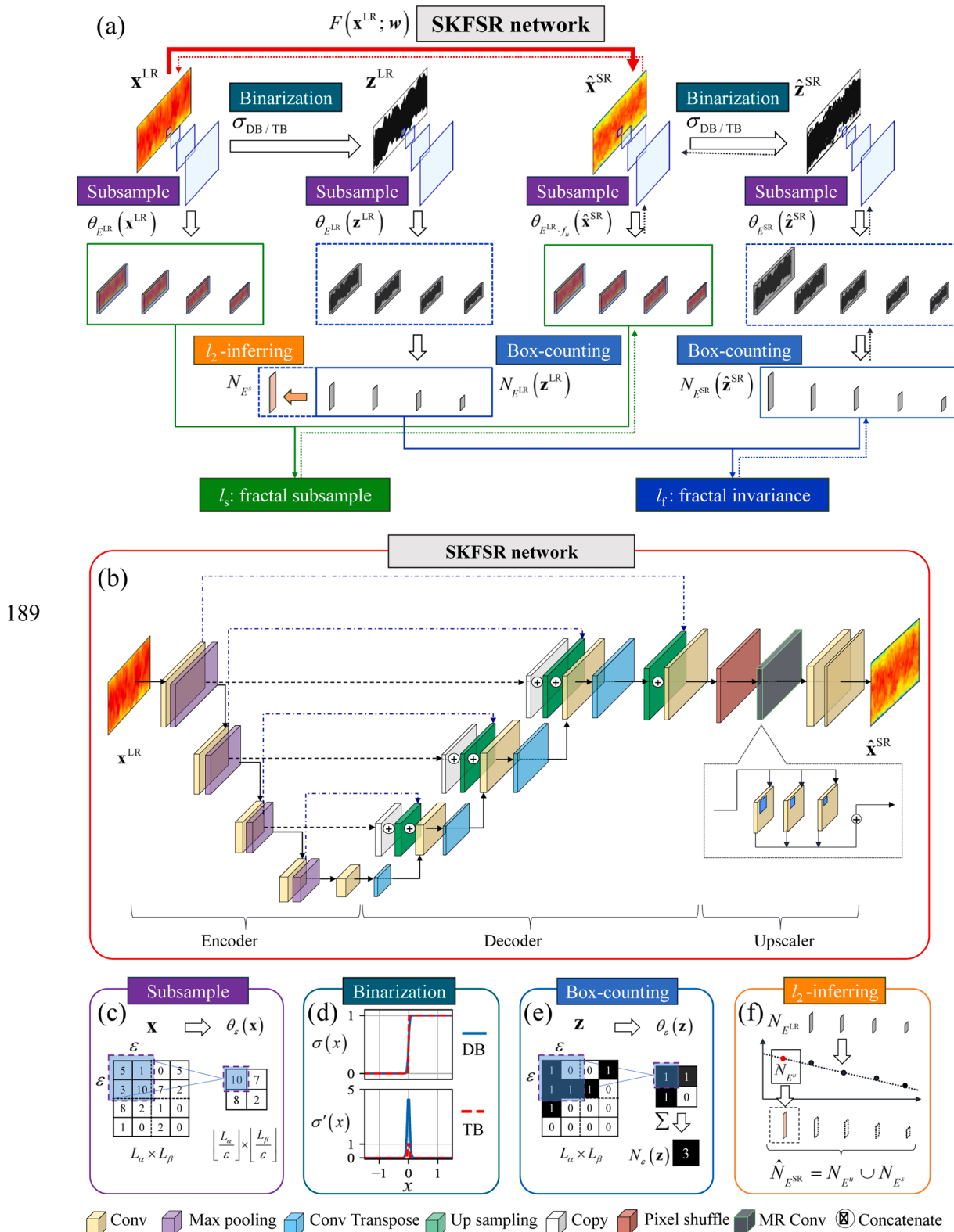


Fig. 2. Schematic illustration of SKFSR-FIC model flow diagram for performing super resolution (a) computational flow diagram of the fractal invariance constraint; (b) SKFSR network architecture; (c) sub-sampling computational unit θ_e ; (d) differential binarization computational unit σ ; (e) tensorized box-counting unit N for computing fractal dimensions; (f) least squares fitting unit.

mechanism on similar geometric structures in multi-scale observations of snapshots, by minimizing the deviation between input LR snapshots and down-samples from HR ones. As indicated by the green arrows in Fig. 2 (a), l_s is evaluated on the LR inputs and HR snapshots that are

down-sampled by using multi-scale windows. This enables the SKFSR network in mining similar spatial features across multiple scales, thereby reducing the dependency on HR samples.

To regularize the feature consistency across different scales, each

down-sampling layer of the SKFSR network applies the max-pooling operation, which is efficient in computation. As illustrated in Fig. 2 (c), each snapshot of dimension $L_\alpha L_\beta$ within the input matrix is divided into $\lfloor L_\alpha / \varepsilon \rfloor \lfloor L_\beta / \varepsilon \rfloor$ sub-regions numbered as P_{ij} , where $\varepsilon \in \mathbb{N}^*$ denotes the size of the square down-sampling window (its moving stride is also ε). In this way, the down-sampled snapshots are represented as

$$\theta_\varepsilon(\mathbf{x})_{ij} = \|\mathbf{x}_{k,l}\|_\infty = \|\mathbf{x}_{i:\varepsilon:(i+1)\cdot\varepsilon, j:\varepsilon:(j+1)\cdot\varepsilon}\|_\infty, \text{ such that } (k, l) \in P_{ij}. \quad (4)$$

where θ_ε denotes the spatial down-sample (with window size ε) method that obtains lower-resolution data from HR ones (i.e., from dimension of $L_\alpha L_\beta$ into $\lfloor L_\alpha / \varepsilon \rfloor \lfloor L_\beta / \varepsilon \rfloor$), such that $\theta_{f_u}(\mathbf{x}^{HR}) \approx \mathbf{x}^{LR}$. Note that θ_ε can be other down-sample techniques such as the average-pooling. The max-pooling is adopted in the present study due to its advantages in retaining the inherent features and structures of HR data, which, hence, exhibits good accuracy in various scenarios of down-sampling. Hence, the input \mathbf{x}^{LR} can be either experimental or numerical data. Moreover, this down-sampling method allows error back propagation and hence provides good accuracy in optimizing the spatial sampling loss function, which is expressed as

$$l_s = \frac{1}{|E^{LR}|} \sum_{\varepsilon \in E^{LR}} \|\theta_{f_u}(\hat{\mathbf{x}}^{SR}) - \theta_\varepsilon(\mathbf{x}^{LR})\|_2^2 + \|\theta_{f_u}(\hat{\mathbf{x}}^{SR}) - \mathbf{x}^{LR}\|_2^2, \quad (5)$$

where E^{LR} denotes the set of boxes (i.e., windows with different sizes) in LR snapshots; θ_{f_u} represents the down-sample with the upscaled window size εf_u . The second term on the right hand side of Eq. (5) represents the increased weight in the loss function for reconstructing information in grids of the smallest scale (i.e., $\varepsilon = 1$ at the HR scale), thereby enhancing the model's ability to reconstruct flow structures corresponding to small scales.

To obtain down-sampled feature maps at different scales that form E^{LR} , several observation windows of size ε are selected within the interval of $[1, \min(L_\alpha, L_\beta)]$. An exponential sequence with base 2 is adopted to determine the window set (denoted by E) for sampling, making the feature maps cover the main flow scales through minimal sampling. The exponential sequence also ensures that the box sizes and their corresponding box-counting numbers are uniformly distributed on the logarithmic axis, enabling a optimal estimation of fractal dimensions (see details in Appendix B). Specifically, the number of windows is determined by the spatial dimensions (i.e., m) of the input snapshots, ranging from 8 to 10 in the cases in this study. Therefore, the two window sets used to obtain the LR- and HR-scale features are $E^{LR} = \{2^0, 2^1, \dots, 2^{\eta^{LR}}\}$ and $E_u = f_u E^{LR} = \{2^{\log_2 f_u}, 2^{1+\log_2 f_u}, \dots, 2^{\eta^{SR}}\}$, respectively, where $\eta^{LR} = \lfloor \log_2 (\min(L_\alpha^{LR}, L_\beta^{LR})) \rfloor$ and $\eta^{SR} = \lfloor \log_2 (\min(L_\alpha^{SR}, L_\beta^{SR})) \rfloor = \log_2 f_u + \eta^{LR}$. Note that the multi-scale spatial sampling loss l_s is computed via ensemble averaging over the LR window set E^{LR} as Eq. (5).

2.2.2. The fractal self-similarity loss l_f

The second part of the loss, i.e., l_f , describes the differences in scale-invariant self-similarities between the LR input snapshots and the reconstructed HR snapshots, as indicated by the blue arrows in Fig. 2 (a). The fractal dimension can be evaluated by a proper box-counting method, which quantifies the scale-invariance correlations between scales and box-counting numbers (i.e., the number of windows that cover a certain area of a dynamic system such as turbulence interfaces). For effectively identifying the geometric structures and interfaces of the studied system, the first step of implementing the box-counting method is binarizing the input snapshots. The present study proposes a Differentiable Binarization (DB) method that is computationally efficient and enables the back propagation of errors, mathematically described as:

$$\mathbf{z} = \sigma_{DB}(\mathbf{x}) = \frac{1}{1 + e^{-\tau(x-T)}}, \quad (6)$$

where \mathbf{z} is the binarized result of each element x of input flow fields to DB layer; τ is a scaling factor and $\tau = 50$ is adopted in this study; the scalar value T is a threshold, which is defined as the mean value of the flow fields that input to the DB layer and does not introduce additional hyperparameters.

The DB method conducts forward computations and effectively binarizes the input snapshots of flow fields, similar to the traditional Truncated Binarization (TB) method, i.e., $\sigma_{TB}(x) = \text{sgn}(\text{sgn}(x - T) + 1)$, as illustrated in Fig. 2 (d). Note that the TB method used in this study adopts an artificial gradient to avoid local non-differentiable extrema. However, these two methods exhibit differences in the derivation computation, which is an essential part during the back propagation of a DL model. Specifically, the function value and derivative mismatch in the TB method due to gradient truncation, which causes information loss during binarization. In contrast, the DB method is globally differentiable in computing derivatives and hence it can accurately recover the flow fields from binary data during backward computations. Therefore, the DB method provides higher accuracy during model optimization and is adopted for computing the FIC proposed in the present study.

With preprocessed data obtained by DB method, the following step is to compute fractal dimensions by using a proper box-counting method. To realize the back propagation during the optimization iteration in deep learning, a tensorized differentiable box-counting strategy is proposed. Specifically, the proposed FIC applies the pooling-based box-counting algorithm, which avoids the nested iterations in traditional fractal dimension computing methods. As illustrated in Fig. 2 (e), by summing up elements in a window ε that partitions the matrix \mathbf{z} , the box-counting number $N_\varepsilon(\mathbf{z})$ corresponding to ε , which covers the partitioned \mathbf{z} , can be computed as

$$N_E(\mathbf{z}) = \left\{ N_\varepsilon | N_\varepsilon = \sum_{j=1}^{\lfloor L_\beta / \varepsilon \rfloor} \sum_{i=1}^{\lfloor L_\alpha / \varepsilon \rfloor} \theta_\varepsilon(\mathbf{z})_{ij}, \varepsilon \in E \right\}, \quad (7)$$

where $N_E(\mathbf{z})$ represents the set of box-counting numbers corresponding to the box set of different scales, i.e., E . Note that max-pooling algorithm with the same window set as that used for computing the loss l_s , i.e., E^{LR} , is applied. In this way, the proposed tensorized box-counting method avoids recursively sliding windows across spatial dimensions that traditional methods do, thereby improving the efficiency during the optimization of the SKFSR network.

By applying the proposed DB and tensorized box-counting method for minimizing l_f (i.e., the back propagation process), the SKFSR-FIC model reconstructs HR snapshots that characterized by the scale-invariant fractal dimensions estimated on the LR inputs. This loss function reads as

$$l_f = \frac{1}{|E^{SR}| L_\alpha L_\beta} \sum_{\varepsilon \in E^{SR}} \left\| N_\varepsilon \left(\underbrace{\sigma(\hat{\mathbf{x}}^{SR})}_{\hat{\mathbf{z}}^{SR}} \right) - \hat{N}_\varepsilon \left(\underbrace{\sigma(\mathbf{x}^{LR})}_{\mathbf{z}^{LR}} \right) \right\|_2^2, \quad (8)$$

where E^{SR} denotes the box set applied to HR snapshots; σ denotes the proposed differential binarization (i.e., the DB method), which processes $\hat{\mathbf{x}}^{SR}$ and \mathbf{x}^{LR} to obtain binary snapshots $\hat{\mathbf{z}}^{SR}$ and \mathbf{z}^{LR} , respectively; N_ε and \hat{N}_ε represent the box-counting number of $\hat{\mathbf{z}}^{SR}$ and \mathbf{z}^{LR} based on the box size ε .

To ensure that the SKFSR model can reconstruct HR snapshots that possess identical self-similarities to the input ones at multiple scales, the set $\hat{N}_{E^{SR}}$ (inferred from the input data) is applied as the reference value. Note that the reference box-counting numbers are computed through taking the union of two separate box-counting number sets, i.e., $\hat{N}_{E^{SR}} = N_{E^u} \cup N_{E^r}$, where $E^u \subset E^{SR}$, and $E^{SR} = \{2^0, 2^1, \dots, 2^{\eta^{SR}}\}$. Specifically for N_{E^u} , the box-counting number of LR snapshots, i.e., $N_{E^{LR}}(\mathbf{z}^{LR})$, is firstly obtained by performing box-counting on \mathbf{x}^{LR} (using boxes of E^{LR}). Due to the scaling relationship between the box-counting numbers of different

scales, the box-counting number sets of the HR snapshots can be efficiently inferred from LR ones via $N_{E^u}(\mathbf{z}^{HR}) = N_{E^{LR}}(\mathbf{z}^{LR})$, where $E^u = f_u E^{LR}$. The other set N_{E^s} (corresponding to the box set $E^s = \mathbb{C}_{E^{SR}} E^u$) can be inferred by using the scale invariance of fractal dimension, as demonstrated by the l_2 -inferring module in Fig. 2 (f), more details are referred to Appendix B.

For short, the proposed FIC allows tensorized computation that can be conducted on GPUs, thereby possessing superior efficiency in computing fractal dimensions. Besides, the proposed loss l_f can accurately back propagate errors and hence address the challenge of traditional DL models where fractal dimensions cannot be used as *a priori* for reconstructing flow fields. Therefore, the FIC significantly improves the efficiency and accuracy of deep learning models in learning and reconstructing fractal features of data.

2.3. Training strategies using data and/or fractal invariance constraint

The physical constraint of FIC and its ease of computation enable the SKFSR-FIC model to conduct zero-shot SR efficiently and accurately, which is termed as the unsupervised learning strategy. Note that the proposed fractal physics-informed strategy is somewhat analogous to PINNs in the aspect of applying physical constraints to enhance the model's accuracy, and the SKFSR-FIC model has released the stringent requirement on using defined governing equations as the physical constraint.

In the scenarios where HR labels are available for training, the proposed SKFSR model can also employ the supervised learning strategy through minimizing L_{data} , i.e., the MSE between the generated SR data and the label HR data, instead of FIC, as presented in Eq. (2). Moreover, by integrating the physical constraint (the fractal invariance here) and HR label data, the SKFSR-FIC model also enables a semi-supervised learning strategy. In this way, the intrinsic features behind the label data provide physical *priori* to the model and hence enhance the extrapolation accuracy. Due to the compatibility of FIC with data, the physics-data combined learning strategy employs a loss function that integrates label data \mathbf{x}^{HR} with FIC (L_{fractal}) as

$$L'_{\text{fractal}} = \frac{1}{|E^{SR}|} \sum_{e \in E^{SR}} \left(\underbrace{\|\theta_e(\mathbf{x}^{HR}) - \theta_e(F(\mathbf{x}^{LR}))\|_2^2}_{l_s^{HR}} + \lambda \underbrace{\|\theta_e(\sigma(\mathbf{x}^{HR})) - \theta_e(\sigma(F(\mathbf{x}^{LR})))\|_2^2}_{l_f^{HR}} \right) \quad (9)$$

Note that l_s^{HR} in Eq. (9) plays the same role as the MSE loss (i.e., L_{data}) when $\epsilon = 1$, but it is computed by incorporating the multi-scale subsamples from HR label data. For computing l_f^{HR} , the box-counting numbers N_e used in Eq. (5) is replaced by the down-sample θ_e , which is advantageous in directly retaining the geometry-related physics of turbulence (as compared to the inferred one by the box-count computation) and hence mitigates numerical errors from the l_2 -norm fitting of the box-counting numbers corresponding to HR scales. This improves the accuracy of HR-scale reconstructions of turbulent flows.

In summary, the FIC is proposed to incorporate the scale invariance as physics into the SKFSR network, leading to the SKFSR-FIC model. The model shines in perceiving the inherent self-similarities behind the

multi-scale structures or patterns of complex fluid flows like turbulence. Besides, the model achieves an adaptive physics-data combined learning, enabling versatile training strategies including the supervised, unsupervised (i.e., zero-shot SR) and semi-supervised learning.

2.4. Numerical implementations and parameter settings

Two error metrics are utilized to evaluate the accuracy of reconstructed HR snapshots within the training and validation (i.e., the ground truth) sets. Firstly, the Root Mean Square Error (RMSE) is applied for assessing the overall spatial-temporal averaged error between the reconstructed data and the ground truth, as

$$\mathcal{E}_s = \frac{1}{m k} \sum_{i=1}^m \sum_{j=1}^k \|\mathbf{x}_{i,j}^{HR} - \hat{\mathbf{x}}_{i,j}^{SR}\|_2, \quad 0 < k < n, \quad (10)$$

where k represents the number of snapshots. The subscripts i and j of snapshots \mathbf{x} denote the spatial and temporal dimensions, respectively.

The second metric estimates the Mean Absolute Error (MAE) between the temporal-averaged fractal dimension of reconstructed data and that of the ground truth, as

$$\mathcal{E}_f = \frac{1}{n} \sum_{j=1}^n \|D_f(\mathbf{x}_{\cdot,j}^{HR}) - D_f(\hat{\mathbf{x}}_{\cdot,j}^{SR})\|_1, \quad (11)$$

where D_f denotes the computed fractal dimension of the studied snapshots, e.g., the label data \mathbf{x}^{HR} and the reconstructed ones $\hat{\mathbf{x}}^{SR}$.

In the SKFSR model, all network layers except for the final output apply the ReLU activation function $\gamma(x) = \max(0, x)$. This allows the SKFSR network to recognize nonlinear features and learn complex mapping relationships for optimizing network weights, where the size of the kernel K is set as 3×3 in each layer. For the weight coefficient λ in FIC, given that the unsupervised learning focuses on reconstructing snapshots with spatial similarities, the λ used for weighting l_f is set to be 0.01, thereby ensuring its minor effect compared to the spatial similarity loss l_s . In semi-supervised learning that applies HR label data instead of inferring them (hence avoiding the underlying errors from l_2 -norm fitting), the λ value of 0.1 is adopted to enhance the contribution of the small-scale features with data to flow reconstructions. For comparing to representative DL models, U-Net, ResNet and FNO are applied in the present study, with the same hyperparameters recommended in Refs [61,62,65] are adopted to obtain good performance of these models (for the ResNet model, the ResNet-101 architecture is adopted). Note that the aforementioned DL models originally cannot be used to conduct SR and do not support unsupervised learning. The FIC module and upscaler proposed in this study are implemented into these DL models to enable unsupervised learning and SR, respectively.

To efficiently optimize the FIC and prevent overfitting, a variant of the adaptive moment estimation called AdamW is utilized and the early stopping criterion is applied for SKFSR and other DLSR models. The tensorized FIC computations, network training, and the online reconstruction of the SKFSR and other DLSR models are based on the PyTorch framework and executed on a workstation equipped with a Nvidia RTX 4090 GPU. The numerical settings of the input data for the cases studied are shown in Table 1. The target resolutions of SR results are set for resolving the inertial flow regime in the energy spectra, where the flow dynamics manifest statistical self-similarities.

Table 1
The input data size and parameters related to offline training for the cases considered in this study.

Case	Target resolution	k	batch size	epochs
Fractal image Fluid Flow	C1a - d	512 × 512	1	1000
	Channel flow (C2a)	512 × 128	1 / 30 / 120	1000
	Isotropic turbulence (C2b)	256 × 256	1 / 8 / 32	1000

3. Results and discussion

The SKFSR model is employed to conduct SR by adaptively imposing the constraint of FIC or MSE loss. Depending on the constraint imposed, different learning strategies can be adopted, i.e., the unsupervised, semi-supervised and supervised learning (denoted as unsp, semi and sup, respectively). The cubic interpolation (categorized as unsupervised learning because no training is required) and compared DLSR models including U-Net, ResNet and FNO, are also implemented for comparison. In this study, two error metrics, i.e., E_s and E_f are applied for evaluating the errors in reconstructing snapshots and self-similarities, respectively. Besides, the probability density function (PDF) and the energy spectra (denoted by E) are analyzed for examining the data distribution and multi-frequency dynamics of the studied systems.

3.1. Cases C1: fractal geometric primitives and iterated images

Fractal geometries generated by predefined primitives with determined and unchanged fractal dimensions are studied to validate the accuracy of the FIC computation. Five primitives are considered and defined as Cases C1 a – e, i.e., a straight line, three Koch curves with different geometric patterns, and the Sierpiński carpet that correspond to the five columns of Fig. 3, respectively. Self-affine fractal images (with strictly invariant self-similarity to the primitives) are generated by the Iterated Function System (IFS; with more details presented in Appendix C). The theoretical fractal dimension can be computed from the initial condition via

$$D_f^{\text{IFS}} = \log(N_{\epsilon^{\text{IFS}}}) / \log(1 / \epsilon^{\text{IFS}}) \quad (12)$$

where ϵ^{IFS} denotes the feature length of each primitive, and $N_{\epsilon^{\text{IFS}}}$ represents the increased number of primitives after each self-affine iteration of IFS. Specifically, the theoretical fractal dimensions of the five considered primitives are 1.00, 1.26, 1.46, 1.50 and 1.85, respectively. The fractal dimension values computed by the proposed tensorized differential box-counting method are 1.00, 1.30, 1.45, 1.50 and 1.85, respectively. For the considered primitives, the deviations between computed and theoretical ones are all within 3%, demonstrating good accuracy in computing the fractal dimension, according to the results from documented studies [66–68].

On the basis of accurate computation of fractal dimension, the unsupervised SR without HR label data is conducted, where $f_u = 8$ is applied in both the SKFSR-based models and the cubic interpolation. In Fig. 3, the 1st row illustrates the predefined five initial primitives. The affined geometries (with iteration numbers shown in Table C.1) corresponding to the LR (64×64) data are illustrated in the 2nd row of Fig. 3. The HR (512×512 , $f_u = 8$) snapshots reconstructed by the cubic interpolation are in the 3rd row, where over smoothed geometries are observed due to the deficiency of interpolation to get the local information. In contrast, the HR fractal snapshots reconstructed by the unsupervised SKFSR-FIC model (see the 4th row of Fig. 3) manifest finer interfaces and better affined structures, due to the incorporation of the scale-invariance of fractal dimension as a constraint. The proposed SKFSR-FIC model overcomes the regional information loss that occurred in the interpolation method, thereby addressing difficulty of reconstructing small-scale structures and retaining the self-similarity of the fractal. This advantage is further illustrated in the 1st row of Fig. 4, where the PDFs of the fractal images reconstructed by SKFSR-FIC are very close to the theoretical ones of HR snapshots, hence demonstrating the enhanced learning capability from non-Gaussian distributed data.

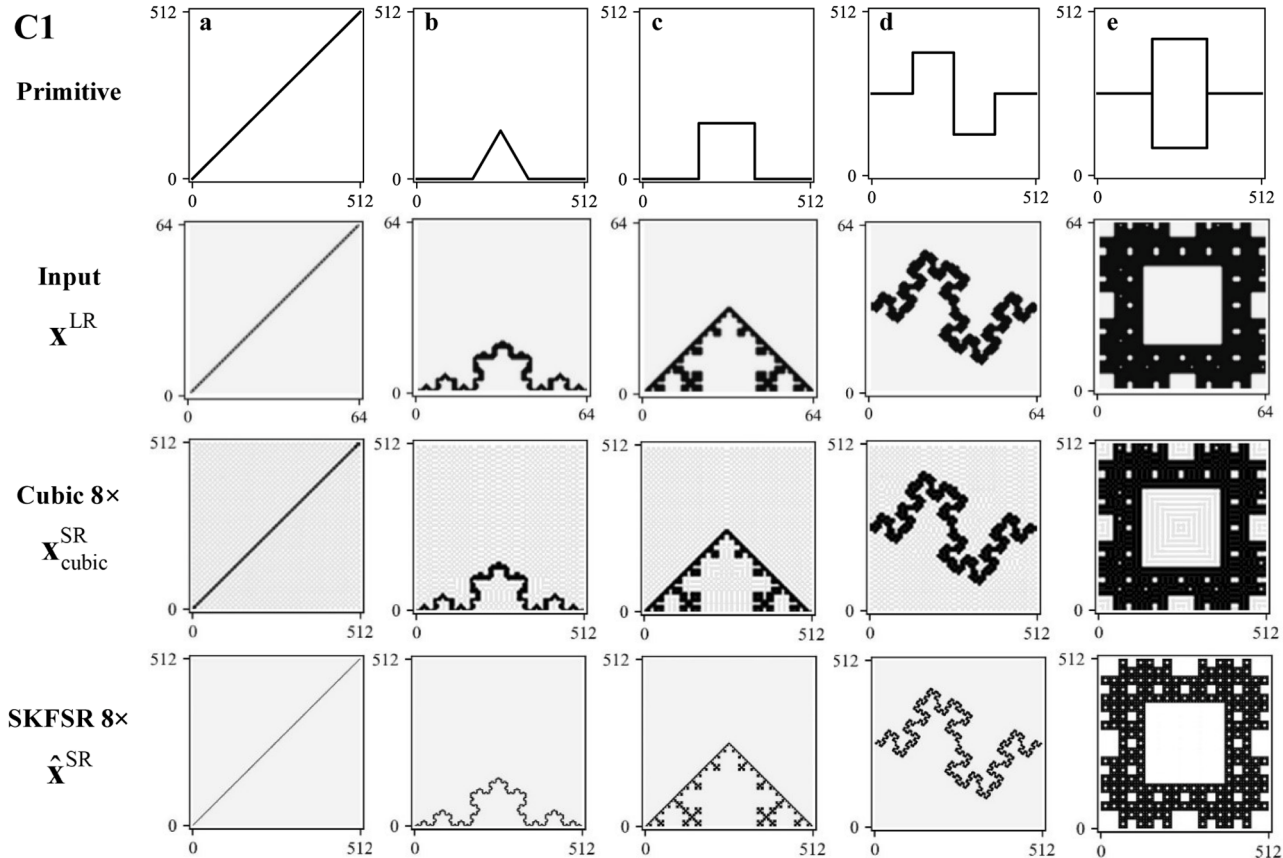


Fig. 3. Schematic view and results of fractal images for the Cases C1. The 1st row: Self-affine primitives, where **a** represents a straight line inclined at 45° , **b**, **c** and **d** are Koch curves of different characteristic lengths and primitive node numbers, and **e** is the Sierpiński carpet. The 2nd row: input LR snapshots. The 3rd row: HR snapshots reconstructed by the cubic interpolation. The 4th row: HR snapshots reconstructed by SKFSR-FIC.

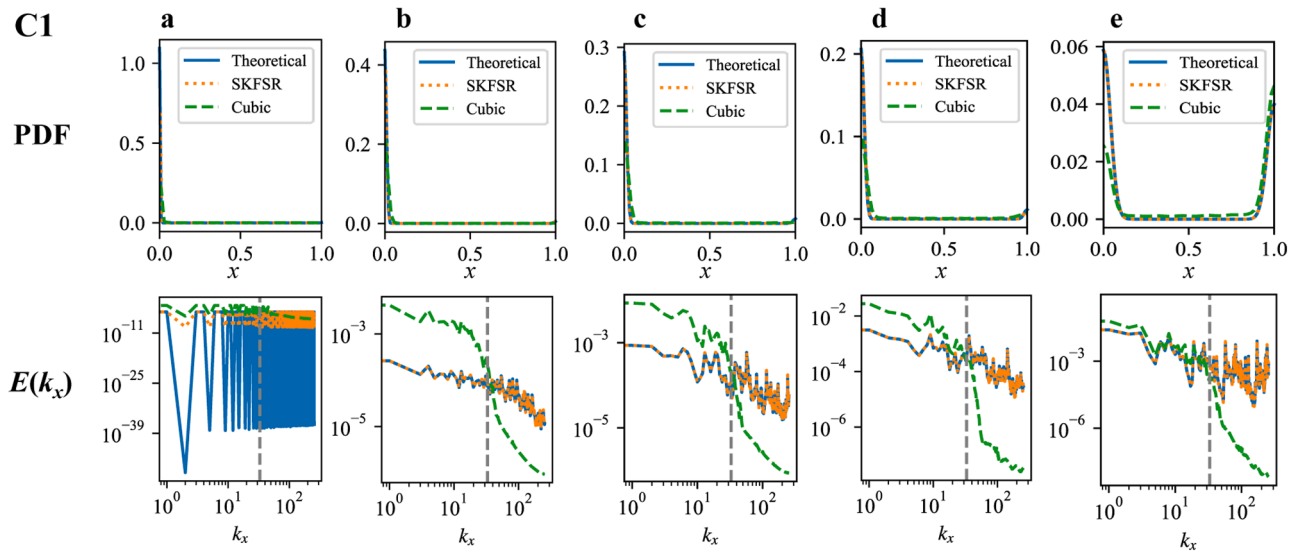


Fig. 4. The results of the fractal images reconstructed by SKFSR-FIC and the cubic interpolation in comparison with the theoretical ones of HR snapshots. The 1st row: probability density functions; The 2nd row: energy spectra curves.

Furthermore, as illustrated in the energy spectra curves in the 2nd of Fig. 4, the SKFSR-FIC shows better reconstruction of the high-frequency information that always presents in smaller scales, which implies that SKFSR-FIC can better recovers information that is missed in LR snapshots.

The spatial-averaged errors of the reconstructed snapshots (denoted by ϵ_s), as well as the deviations between the theoretical fractal dimensions and the computed ones of SR outputs (denoted by ϵ_f), are analyzed. Table 2 shows that the accuracy of the unsupervised SKFSR-FIC in reconstructing spatial information is improved by three orders of magnitude compared to the cubic interpolation. This further leads to a significantly enhanced enforcement of the self-similarity of geometries during SR, as indicated by the ϵ_f values that are one to two orders of magnitude reduced. As compared to other three DLSR models (i.e., FNO, U-Net and ResNet), SKFSR-FIC also outperforms by two to three orders of magnitude in accuracy. The above results demonstrate the advantage of the SKFSR network architecture on handling fractals. In terms of computational efficiency, SKFSR-FIC achieves three times improvements as compared to the interpolation method and at least 20% speed-up in offline training compared to other DLSR models considered. Furthermore, how the parameter settings of the FIC affect the SR results

are examined. As shown at the bottom of Table 2, the numerical error of the result by the adopted FIC setting is 10% to one thousand times smaller compared to other parameter settings, demonstrating the rationality of the adopted FIC settings. To sum-up, the proposed FIC is capable of computing fractal dimensions of various primitive geometries accurately and efficiently, the integration of which with the SKFSR network that excels at perceiving multi-scale features enable high-precision SR even without HR labels.

3.2. Cases C2: chaotic turbulence

The SR of two cases of turbulent flows with statistical self-similarity is conducted. The two cases are the channel turbulent flow (Case C2a) and isotropic turbulence in a periodic square region (Case C2b). The Direct Numerical Simulation (DNS) data of both cases are downloaded from the turbulence database of Johns Hopkins University and each case contains 150 time-snapshots. The snapshot data are subsampled and serve as the LR input, where only low-frequency components in the energy spectra (i.e., the mean-flows and the transition regime to inertial flows) are retained. In the super resolution, the upscaling factors of $f_u = 2, 4$ and 8 are considered. On these resolutions, the fluid flows include

Table 2

Computational errors and time for the five fractal geometric cases, and computational errors corresponding to different parameter modifications in FIC (taking C1e as an example).

Case	Computational errors and time					Time (s)		
	C1a	C1b	C1c	C1d	C1e			
SKFSR	6.27×10^{-4}	4.68×10^{-4}	3.70×10^{-4}	9.25×10^{-4}	3.20×10^{-4}	69.32	0.08	0.01
	0.05	0.00	0.00	0.00	0.00			
FNO	9.67×10^{-2}	9.70×10^{-2}	9.68×10^{-2}	9.72×10^{-2}	7.64×10^{-2}	98.12	0.13	0.01
	0.96	0.63	0.47	0.32	0.00			
U-Net	2.83×10^{-2}	2.82×10^{-2}	2.93×10^{-2}	3.01×10^{-2}	7.16×10^{-2}	96.24	0.10	0.01
	0.95	0.57	0.03	0.00	0.00			
ResNet	3.97×10^{-1}	3.71×10^{-1}	5.89×10^{-1}	5.20×10^{-1}	5.95×10^{-1}	233.26	0.23	0.02
	0.96	0.66	0.52	0.47	0.01			
Cubic	3.13×10^{-1}	1.86×10^{-1}	2.43×10^{-1}	3.13×10^{-1}	3.93×10^{-1}	/	/	0.03
	0.27	0.42	0.33	0.27	0.02			
Computational errors corresponding to different parameter modifications in FIC								
Method	Proposed FIC	Avg pooling	Remove l_s	Remove l_f	Remove l_2 -inferring			
ϵ_s	3.20×10^{-4}	8.18×10^{-4}	7.55×10^{-4}	4.66×10^{-1}	3.54×10^{-4}			

the components in the inertial subrange, which possess statistical self-similar flow structures. For the unsupervised learning strategy, only LR snapshots are applied in the offline training of the SKFSR-FIC model and the numbers of snapshots used for training are $k = 1, 30$ and 120 , corresponding to the single, few and standard quantities of snapshots, respectively. In the supervised and semi-supervised learning, k (the same values as above) pieces of HR samples are used as labels. Note that the first snapshot of each case, i.e., initial state of the flow field, is selected for minimizing the loss functions corresponding to SKFSR-FIC and other DLSR models. The spatial-temporal averaged errors of the computational results with respect to the training time sequence are denoted by $\epsilon_s^{\text{recon}}$, and the errors corresponding to the results beyond the training set (i.e., extrapolation sets) ϵ_s^{pred} . The total computational time for the offline training is denoted as T_{offline} , the average time per training epoch denoted as T_{epoch} , and the time for the online computation of performing SR (with established models) denoted as T_{online} .

As shown in [Tables 3 and 4](#), the SKFSR-FIC model trained in unsupervised learning achieves 50% accuracy improvement in snapshot reconstruction compared to the cubic interpolation and a two-times improvement compared to the three considered DLSR models. In terms of minimizing the errors of the fractal dimension, i.e., ϵ_f , the unsupervised SKFSR-FIC improves the results by at least two orders of magnitude compared to the cubic interpolation, demonstrating the necessity and immediate effect of retaining self-similarity in the SR of turbulent flows. By imposing the MSE loss (with respect to the label data) instead of the FIC, the supervised SKFSR model still surpasses DLSR models in accuracy, and particularly for the reconstruction results, the numerical errors $\epsilon_s^{\text{recon}}$ are ten times smaller. This highlights the superior data mining capability provided by the multi-scale perceptive network in the SKFSR model. For the SKFSR-FIC with semi-supervised learning (i.e., integrating HR data and FIC to identify scale invariants), its accuracy in extrapolation is at least two times higher compared to other DLSR models. These results indicate that the SKFSR models utilizing three learning strategies all achieve significantly improved accuracy in SR reconstructions of turbulent flows and in keeping the fractal dimensions of flow structures under the upscaling factors up to 8. This is attributed to the adaptive physics-data combined learning strategy, which helps learn and extract spatial-temporal fractal invariants from data.

Another notable advantage of the proposed FIC lies in that it reduces the reliance of DLSR models on label data. As shown in [Tables 3 and 4](#), for the DLSR models applying the MSE loss instead of FIC (i.e.,

supervised-learning models), the numerical errors corresponding to the extrapolated results, i.e., ϵ_s^{pred} , is up to 10 times higher than those for the results covered by the training sets i.e., $\epsilon_s^{\text{recon}}$ (taking the case of $k = 1$ as an example). This accuracy degradation for extrapolation is related to the overfitting issue of the supervised learning, which implies that an over complex mapping function is trained for the highly nonlinear turbulent flow. By increasing the training snapshots to $k = 30$ and 120 , the extrapolation errors ϵ_s^{pred} of the considered supervised DLSR models (taking SKFSR as an example) decrease by 10% and 15%, respectively. It means the improvement in extrapolation accuracy is marginal with the increase of training snapshots, but the HR training data and computational resources are significantly increased. In contrast, the unsupervised and semi-supervised models incorporating FIC, i.e., the SKFSR-FIC models, mitigate the extrapolation errors ϵ_s^{pred} in the two considered cases (estimated with supervised learning strategy) by 20%. This indicates the effectiveness of FIC in overcoming the overfitting issue existing in the supervised learning DLSR models without FIC. Also, the accuracy of the unsupervised SKFSR-FIC is comparable to or even surpasses that of other supervised DLSR models employing 30 and 120 HR snapshots, demonstrating that the physics retained by FIC offers benefit in reducing the demand of data. On the basis of the model with the physical constraint of FIC, the model's accuracy can be further improved by integrating HR data (even as few as one snapshot), i.e., the semi-supervised SKFSR-FIC model. Specifically, the semi-supervised SKFSR-FIC achieves 20% improvement in extrapolation accuracy compared to the SKFSR-FIC model without HR data input.

For spatial flow structure in turbulence, results of Cases C2a and C2b in [Figs. 5 and 6](#) show that (taking the results of $f_u = 8$ as an example) the SKFSR-FIC models, especially that trained by semi-supervised learning, well reconstruct the coherent flow structures across multiple scales. Specifically for the channel turbulent flow case, the boundary layers near walls and smaller-scale flows such as plumes detaching and moving towards the channel center are satisfactorily reconstructed. In the case of isotropic turbulence, flows of relatively large scales are mainly clustered in the intermediate horizontal strip area of the domain and are of relatively higher velocities; small-scale flow structures are scattered in the whole domain characterized by fluctuating velocities. Note that the small-scale dynamics reconstructed by the SKFSR-FIC models are close to the ground truth, while such structures in the results by traditional DLSR models and the interpolation method are either noisy due to overfitting issue or oversmoothed because high-frequency components are filtered out. This demonstrates the advantage of SKFSR-FIC models

Table 3

Spatial-temporal averaged errors and self-similarity errors of different SR models in reconstructing the horizontal velocities in the cases of channel turbulent flow (C2a).

	C2a	$f_u = 2$	$f_u = 4$			$f_u = 8$				
			k	$\epsilon_s^{\text{recon}}$	ϵ_s^{pred}	ϵ_f	$\epsilon_s^{\text{recon}}$	ϵ_s^{pred}	ϵ_f	
SKFSR	unsp	1	0.035	0.036	0.003	0.063	0.063	0.008	0.082	0.082
		30	0.037	0.037	0.005	0.061	0.061	0.006	0.079	0.079
		120	0.036	0.036	0.004	0.065	0.065	0.009	0.086	0.087
	sup	1	0.003	0.033	0.003	0.009	0.053	0.002	0.016	0.070
		30	0.013	0.031	0.002	0.026	0.051	0.001	0.033	0.064
		120	0.013	0.029	0.000	0.023	0.045	0.002	0.030	0.059
U-Net	semi	1	0.016	0.029	0.001	0.024	0.049	0.002	0.028	0.068
		30	0.023	0.026	0.001	0.035	0.044	0.001	0.041	0.064
		120	0.020	0.026	0.000	0.033	0.043	0.000	0.040	0.059
	unsp	120	0.057	0.058	0.007	0.293	0.292	0.013	0.172	0.172
		sup	120	0.023	0.030	0.001	0.032	0.045	0.003	0.042
		sup	120	0.053	0.054	0.001	0.107	0.107	0.009	0.066
FNO	unsp	120	0.067	0.067	0.007	0.258	0.258	0.011	0.871	0.871
		sup	120	0.023	0.034	0.001	0.032	0.054	0.004	0.043
	semi	120	0.031	0.037	0.002	0.054	0.062	0.003	0.055	0.065
		unsp	120	0.095	0.110	0.001	0.268	0.268	0.020	0.630
ResNet	sup	120	0.039	0.078	0.002	0.036	0.077	0.003	0.071	0.077
	semi	120	0.070	0.088	0.002	0.059	0.085	0.002	0.065	0.086
Cubic	unsp	/	0.088	0.088	0.101	0.127	0.127	0.045	0.163	0.164
										0.019

Table 4

Spatial-temporal averaged errors and self-similarity errors of different SR models in reconstructing the horizontal velocities in the cases of isotropic turbulence (C2b).

C2b	k	$f_u = 2$			$f_u = 4$			$f_u = 8$			
		$\epsilon_s^{\text{recon}}$	ϵ_s^{pred}	ϵ_f	$\epsilon_s^{\text{recon}}$	ϵ_s^{pred}	ϵ_f	$\epsilon_s^{\text{recon}}$	ϵ_s^{pred}	ϵ_f	
SKFSR	1	0.129	0.137	0.005	0.335	0.392	0.002	0.317	0.335	0.001	
	30	0.151	0.155	0.000	0.328	0.365	0.012	0.320	0.325	0.011	
	120	0.163	0.164	0.001	0.267	0.256	0.021	0.460	0.500	0.049	
	1	0.012	0.130	0.001	0.037	0.254	0.001	0.059	0.356	0.009	
	30	0.074	0.116	0.005	0.126	0.251	0.007	0.134	0.370	0.011	
	120	0.070	0.113	0.001	0.114	0.213	0.008	0.138	0.315	0.010	
U-Net	1	0.087	0.109	0.003	0.088	0.237	0.001	0.122	0.354	0.002	
	30	0.101	0.108	0.002	0.175	0.197	0.000	0.181	0.351	0.004	
	120	0.105	0.102	0.003	0.157	0.196	0.002	0.176	0.302	0.001	
	120	1.182	1.128	0.079	2.399	2.753	0.098	1.874	2.155	0.116	
	120	0.120	0.123	0.005	0.184	0.200	0.011	0.213	0.300	0.017	
	120	0.151	0.146	0.002	0.313	0.286	0.015	0.315	0.313	0.012	
FNO	120	0.370	0.385	0.026	2.971	3.175	0.079	10.937	12.061	0.107	
	120	0.092	0.214	0.004	0.438	0.603	0.012	0.207	0.426	0.018	
	120	0.170	0.196	0.005	0.245	0.297	0.009	0.257	0.307	0.004	
ResNet	120	1.614	1.958	0.004	1.744	1.819	0.080	2.759	2.593	0.088	
	120	0.462	0.614	0.006	0.438	0.603	0.012	0.511	0.614	0.013	
	120	0.496	0.623	0.022	0.447	0.626	0.012	0.494	0.640	0.002	
Cubic	unsp	/	0.218	0.218	0.026	0.375	0.375	0.047	0.587	0.562	0.031

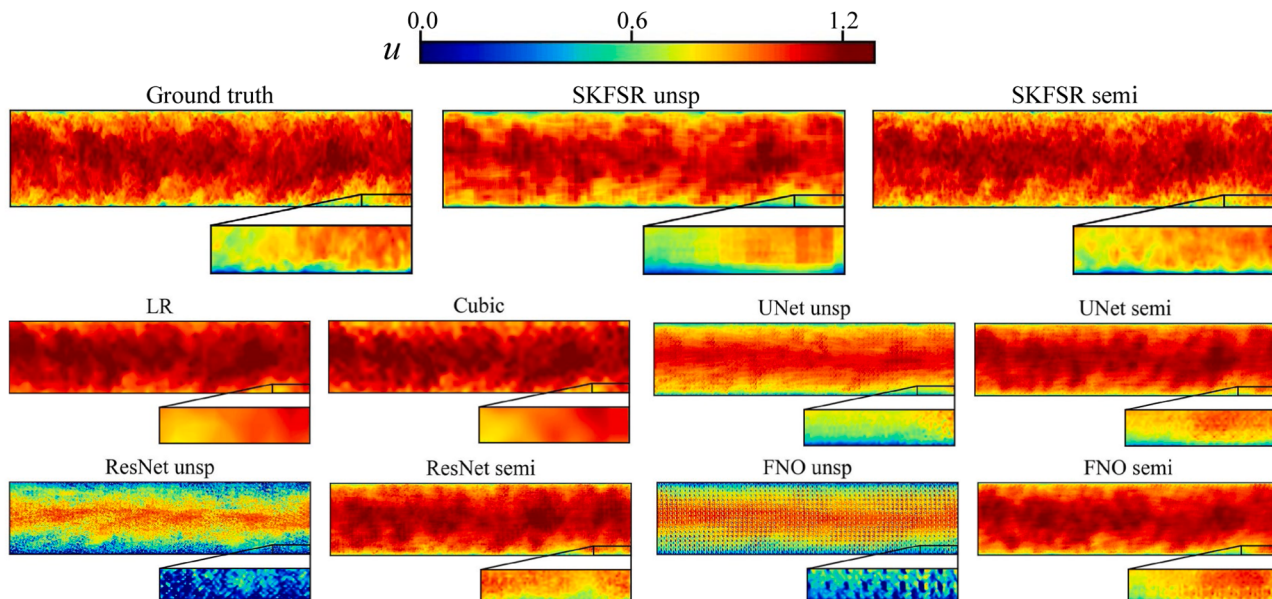


Fig. 5. Contours of the horizontal velocity u reconstructed by the unsupervised and semi-supervised models with $f_u = 8$ in Case C2a.

in capturing multi-scale physics, especially in reconstructing small-scale flow structures.

The energy spectra of the reconstructed velocity (on x -direction) fields versus wavenumber are presented in Figs. 7 and 8, where a larger wavenumber k_x corresponds to a larger frequency and smaller scale of a certain flow structure. Over 90% of the kinetic energy associated with relatively large-scale flows (corresponding to the first 10% of k_x in ascending order) is successfully reconstructed by the considered DLSR models, while the cubic interpolation produces a faster decline or more dissipative spectra because small-scale flow structures are numerically removed during the interpolation process. Regarding the inertial sub-range (the area to the right of gray dashed lines in the figures), the energy spectra curves corresponding to other DLSR models show unphysical rises. This implies the energy increases with the decrease of the turbulence scale, which is contrary to the energy cascade of turbulence.

Specifically for the energy spectra of the small-scale flow regimes (e.g., $k_x \geq 32$ and 16 respectively for Cases C2a and C2b), the SKFSR-FIC

models achieve up to one thousand times higher accuracy compared to the interpolation method that cannot retain the high-frequency or small-scale flow components. Note that in these k_x ranges, the flows are in the inertial subrange and the transition regime to inertial flows and manifest self-similarities in turbulence transport and diffusion [69], which are retained and successfully reproduced by SKFSR-FIC. Also, the SKFSR-FIC models mitigate the unphysical fluctuations of the energy spectra produced by other DLSR models and, quantitatively, they achieve up to 100 times higher accuracy. These demonstrate that the SKFSR-FIC models, especially that with semi-supervised learning, can satisfactorily reproduce the power law of the energy spectrum in the inertial subrange. This superior accuracy owes to FIC that harnesses the inherent self-similarity from the direct energy cascades, and hence mitigates the unphysical fluctuations in reproducing the high-frequency dynamics that can be incurred by the overfitting of traditional DLSR models.

Owing to the accurate reconstruction of multi-scale fluid dynamics, the PDFs of the flow velocities (see Figs. 9 and 10) reconstructed by all

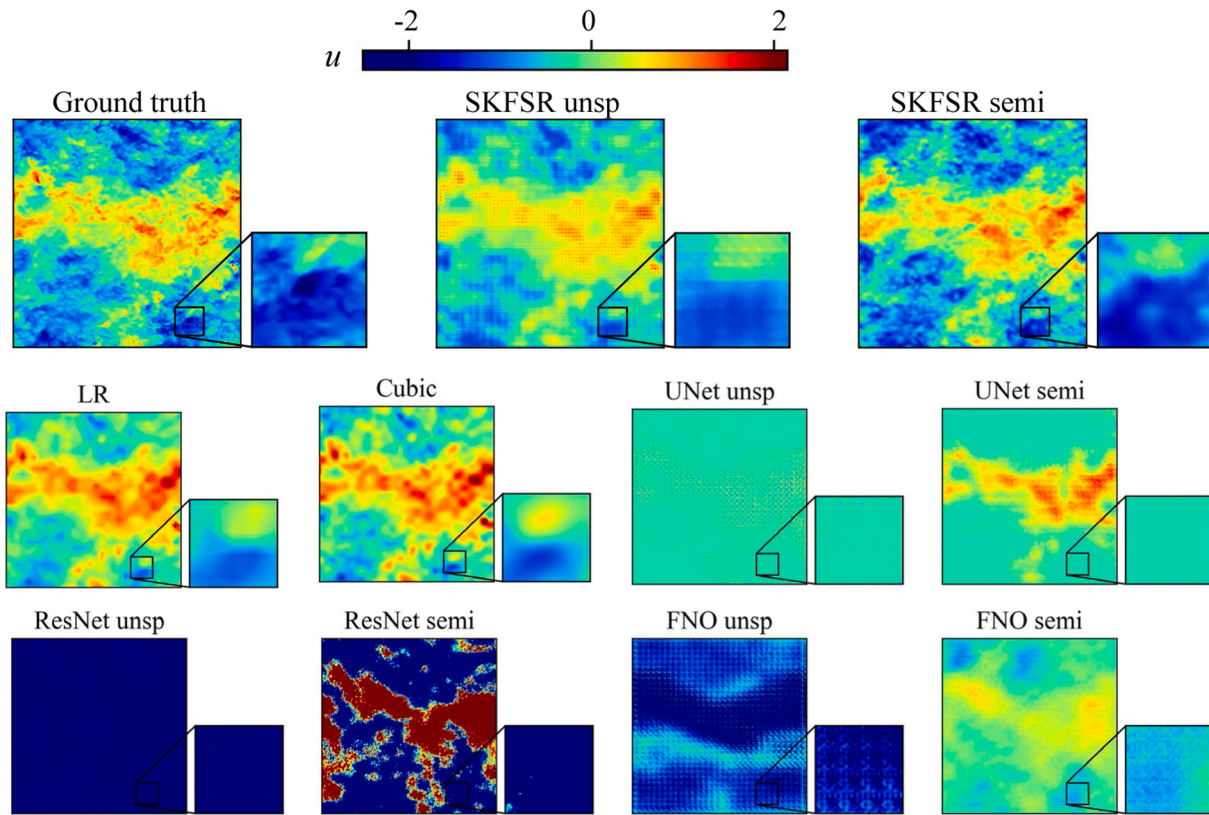


Fig. 6. Contours of the horizontal velocity u reconstructed by the unsupervised and semi-supervised models with $f_u = 8$ in Case C2b.

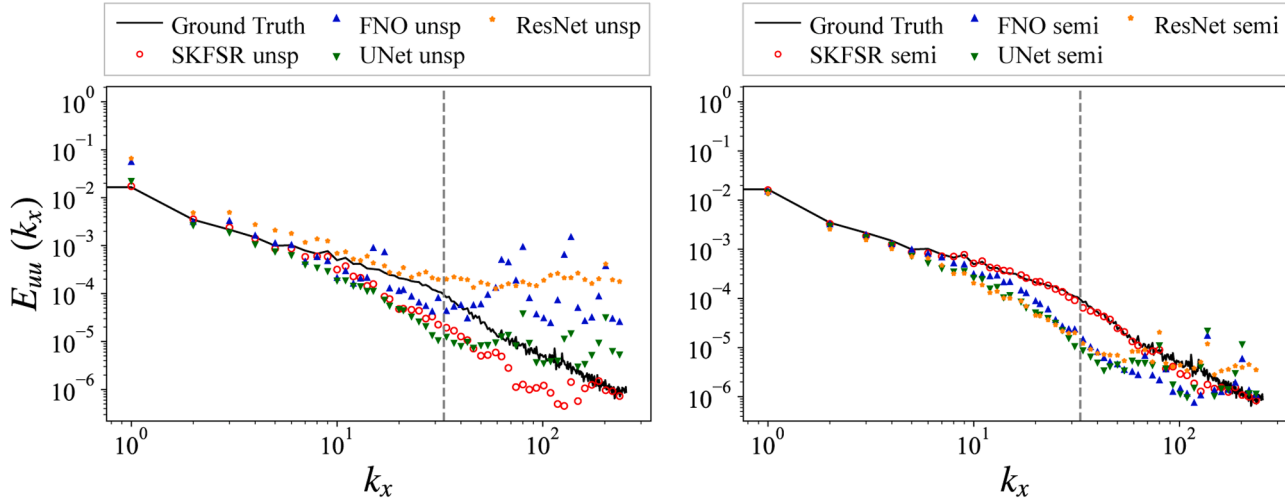


Fig. 7. Turbulent kinetic energy versus k_x that indicates scales of flow structures, where the gray vertical line indicates the highest frequencies captured in LR data of Case C2a.

the SKFSR-FIC models well match the ground truth in terms of the overall shape and peak values, although the semi-supervised model shows the highest accuracy. In contrast, the PDFs of other DLSR models show shifted peaks due to the issue of overfitting multi-scale physics. Compared to the interpolation method, SKFSR-FIC models reconstruct such velocity distributions whose velocity range is up to two times wider, implying more flow information is retained. Regarding the flow velocities with higher probabilities (related to mean velocity that dominates the flow features), the SKFSR-FIC models achieve up to 2-times higher reconstruction accuracy than the DLSR models and surpass interpolation method by 5 times at maximum. For velocities with

relatively low probabilities (e.g., below 0.7 and -1.5 in Cases C2a and C2b, respectively), all SKFSR-FIC models well resolve the corresponding fluctuations, while such small-scale flow structures are numerically smeared out in the results by other models. This demonstrates the distinguished capability of SKFSR-FIC models in retaining multi-scale flow components and reconstructing flow statistics associated with intermittencies of turbulence.

In short, the SKFSR-FIC models, through applying physics of flow fractal structure, enable accurate and efficient reconstruction of highly-nonlinear fluid flows with multi-scale dynamics, as well as reduces the requirements on input data, achieving zero- / one-shot SR.

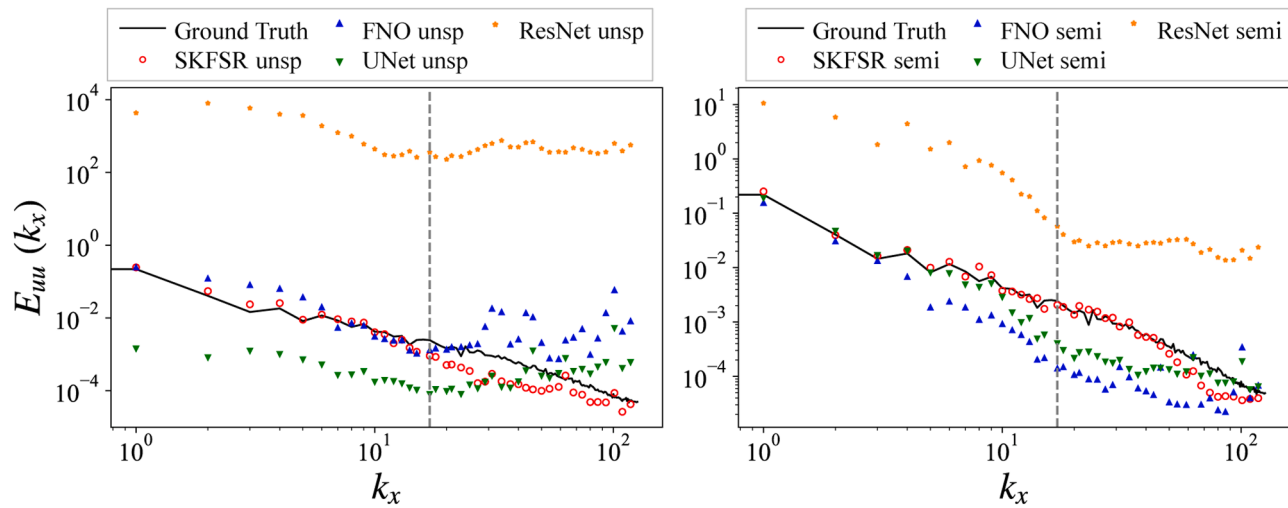


Fig. 8. Turbulent kinetic energy versus k_x that indicates scales of flow structures, where the gray vertical line indicates the highest frequencies captured in LR data of Case C2b.

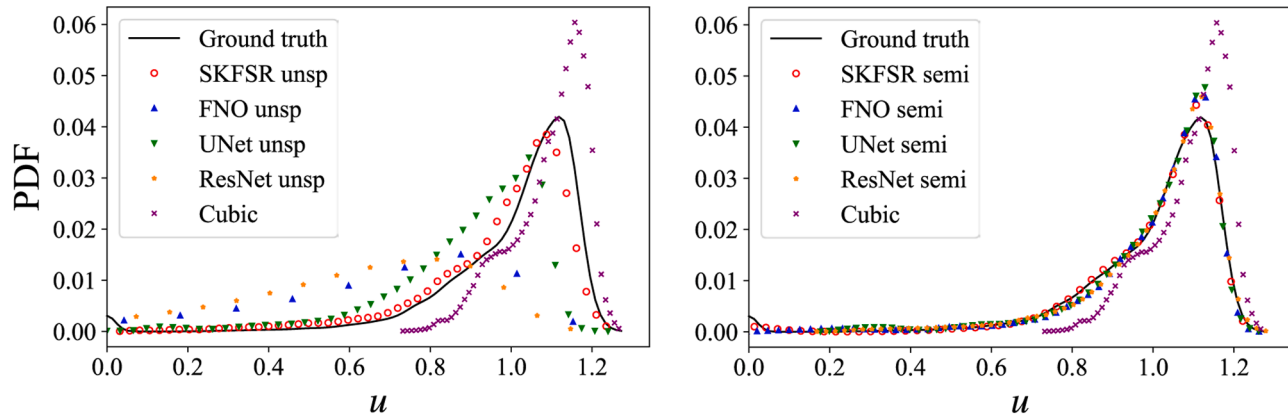


Fig. 9. Probability density function versus flow velocity u reconstructed by the unsupervised (left) and semi-supervised models (right) in Case C2a.

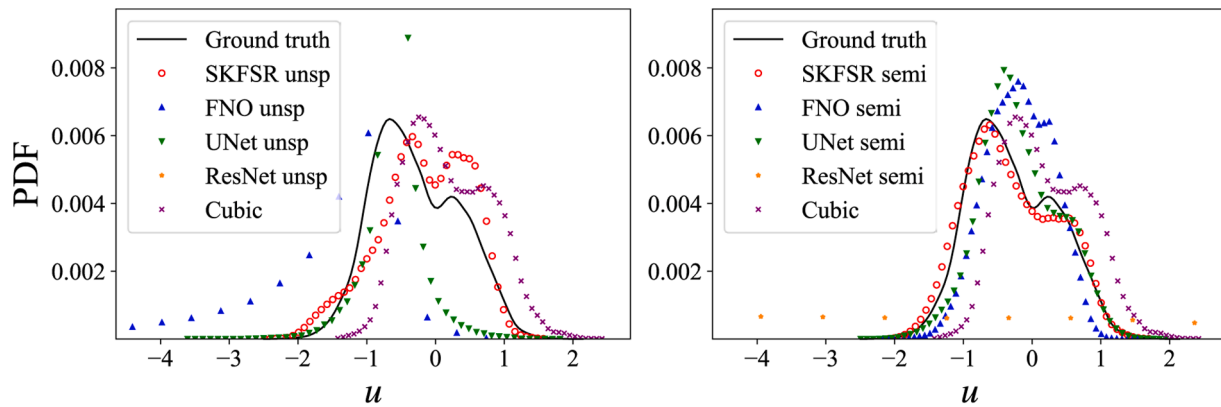


Fig. 10. Probability density function versus flow velocity u reconstructed by the unsupervised (left) and semi-supervised models (right) in Case C2b.

4. Conclusions and future perspectives

The study proposes a deep network SKFSR and a fractal invariance constraint, and integrates them to develop the SKFSR-FIC models for accurate and efficient super-resolution of highly-nonlinear dynamic flows like turbulence. The deep network SKFSR, characterized by the multi-scale feature identification and reuse, can retain a broad range of

scale or frequency components for learning and reconstructing flow statistics and physics, which is essential for super resolution of highly-nonlinear dynamic flows. The FIC, featured with a newly-proposed differentiable box-counting algorithm, efficiently computes the fractal dimension and overcomes the issue of error back propagation in traditional approaches. Besides, the FIC imposes the physics of scale-invariance and hence reduces the reliance of the SKFSR-FIC models on

HR label data, especially in handling turbulent flow scenarios beyond the training dataset, i.e., extrapolation. Moreover, the SKFSR models can flexibly utilize FIC and label data and hence enable adaptive learning strategies, including unsupervised, supervised and semi-supervised learning. Among the three learning strategies, the semi-supervised SKFSR-FIC model incorporates physics and data and shows the best accuracy even when the label data of one snapshot is used (i.e., one-shot SR).

The advantageous features of the SKFSR-FIC models are firstly demonstrated by reconstructing five self-affined fractal images. The accuracy of the zero-shot SKFSR-FIC surpasses other DLSR models and the interpolation method by up to three orders of magnitude, indicating that the learnt self-similarities help reconstruct complex geometries and reduces the reliance of the model on label data. The online computational efficiency of SKFSR-FIC is three times higher than the interpolation method and the offline training efficiency is approximately 20% better than those of other DLSR models that lacks multi-scale reuse and upscaling. Then, two turbulent flow cases driven by different boundary conditions are studied. The SKFSR-FIC models that use zero or one snapshot data show up to three times higher accuracy in reconstructing the velocity fields than other DLSR models utilizing 120 HR snapshots. Besides, the SKFSR-FIC models significantly enhance the accuracy in reproducing the distribution of turbulence kinetic energy versus flow scales, specifically mitigating the unphysical fluctuations in the energy curves by other DLSR models and the over-smoothing of high-frequency components by the interpolation method. Moreover, the SKFSR-FIC models demonstrate five times higher accuracy in reproducing the probability distribution of turbulent flow velocities. The superior accuracy and efficiency are mainly attributed to the SKFSR network that identifies multi-scale fractal structures for super resolution and the FIC that learns and incorporates the inherent scale-invariant physics. The enhanced performances of SKFSR advance the up-to-date theories and technologies in super resolution of turbulent flows.

Note that the present study only considers flow scales until the inertial subrange; hence, one future work is to reconstruct flows to finer resolutions such that the flow information in the dissipation subrange (where flows are isotropic and exhibit self-similarity) can be reproduced. Besides, the physics-data combined feature of the proposed SKFSR-FIC have relaxed the reliance on prior knowledge and data and, hence, are suitable for handling complex systems without defined governing equations. Therefore, another future research direction is to extend the applicability of SKFSR-FIC through combining the intrinsic self-similarities of complex, and always undefined, systems with

observation data. This will advance the prediction and revelation of such systems, like tropical cyclone evolution, coastline change, etc.

Data availability

The fractal images of Cases C1a - e are generated by using the IFS, and the DNS data of Cases C2a and C2b are downloaded from Johns Hopkins Turbulence Databases (<https://turbulence.pha.jhu.edu/>). Sample codes and data supporting the study results are available on GitHub repository (<https://github.com/mlfluids-wjx/SKFSR>). Other data that support the findings of this study can be obtained from the corresponding author upon reasonable request.

CRediT authorship contribution statement

Jixin Wu: Writing – review & editing, Writing – original draft, Visualization, Validation, Software, Methodology, Investigation, Formal analysis, Data curation, Conceptualization. **Min Luo:** Writing – review & editing, Writing – original draft, Visualization, Validation, Supervision, Resources, Project administration, Methodology, Investigation, Funding acquisition, Formal analysis, Conceptualization. **Boo Cheong Khoo:** Writing – review & editing, Supervision, Methodology, Conceptualization. **Dunhui Xiao:** Writing – review & editing, Validation, Methodology, Conceptualization. **Pengzhi Lin:** Writing – review & editing, Methodology, Conceptualization.

Declaration of competing interest

The authors declare that they have no known competing financial interests or personal relationships that could have appeared to influence the work reported in this paper.

Acknowledgements

This research was partially supported by the National Key R&D Program of China (Grant No. 2023YFC3081300), the National Natural Science Foundation of China (Grant No. 12302319), and the start-up funding provided by Zhejiang University (to the corresponding author). The first author acknowledges the financial support of the China Scholarship Council (No. 202306320369) during his visit at the National University of Singapore. The authors would like to thank the technical supports from the HPC center at the Zhoushan Campus of Zhejiang University.

Appendix A. Trainable parameters of the SKFSR network

Convolutional layers with trainable parameters are the basic components that constituting the SKFSR network. With data input into the convolutional layers, the feature maps of different scales are concatenated for implementing feature reuse. In order from input to output, the parameters related to the convolutional layers of SKFSR network are presented in Table A.1 (taking Case C2a with $f_u = 8$ as an example). Specifically for the encoder of SKFSR, five convolutional layers are applied for obtaining feature maps of different scales. In the decoder, five convolutional layers and deconvolutional layers (with the same parameters as that in encoder) are applied for obtaining high-resolution feature maps. In the upscaler, the decoded feature maps are firstly fed into PS layer, which upscales the spatial resolution of data. For perceiving multi-scale features, the upscaler applies a MRConv unit that consisting of three convolutional layers, with their kernels being 3×3 , 5×5 and 7×7 . The following is one convolutional layer for merging the feature maps of different scales, and the final output layer.

Table A.1

Trainable parameters in the convolutional layers for Case C2a, where the input spatial resolution is 64×16 , the input is the velocity field.

Layer #	Encoder		Decoder		Upscaler	
	Input	Output	Input	Output	Input	Output
1	$64 \times 16 \times 1$	$64 \times 16 \times 32$	$8 \times 2 \times 512$	$8 \times 2 \times 256$	$512 \times 128 \times 2$	$512 \times 128 \times 32$
2	$32 \times 8 \times 32$	$32 \times 8 \times 64$	$16 \times 4 \times 512$	$16 \times 4 \times 256$	$512 \times 128 \times 2$	$512 \times 128 \times 32$
3	$16 \times 4 \times 64$	$16 \times 4 \times 128$	$32 \times 8 \times 320$	$32 \times 8 \times 128$	$512 \times 128 \times 2$	$512 \times 128 \times 32$
4	$8 \times 2 \times 128$	$8 \times 2 \times 256$	$64 \times 16 \times 160$	$64 \times 16 \times 64$	$512 \times 128 \times 96$	$512 \times 128 \times 64$
5	$4 \times 1 \times 256$	$4 \times 1 \times 512$	$128 \times 32 \times 64$	$128 \times 32 \times 32$	$512 \times 128 \times 64$	$512 \times 128 \times 1$

Appendix B. Implementation of the l_2 -inferring module

The fractal dimensions describe the scaling relationship between box-counting numbers and scales. Hence, the box-counting number of \mathbf{x}^{HR} (i.e., N_{E^s}) and can be inferred by using the scale-invariance of fractal dimension. According to the fractal theory, the fractal dimension D_f quantifies the approximately linear ratio between N_ε and ε in the logarithmic scale. Specifically, D_f can be computed based on \mathbf{x}^{LR} as

$$D_f = \underset{\alpha}{\operatorname{argmin}} \sum_{\varepsilon \in E^{\text{LR}}} \left\| \underbrace{\log(N_\varepsilon) - \alpha \log\left(\frac{1}{\varepsilon}\right)}_C \right\|_2^2, \quad (\text{B.1})$$

where $C_f = \lim_{\varepsilon \rightarrow 0} C$ represents the intercept in the logarithmic scale. Eq. (B.1) can be efficiently solved by using the least square methods, as illustrated in Fig. 2 (f). Due to the scale-invariance, i.e., D_f obtained from different observation scales are invariant or statistically equal, i.e., D_f of \mathbf{x}^{LR} equals that of \mathbf{x}^{HR} . Hence, the box-counting numbers N_{E^s} relating to the remaining boxes $E^s = \mathcal{C}_{E^s} E^u$ can be fitted in l_2 -norm via

$$N_{E^s}(\mathbf{z}) = \{N_\varepsilon \mid N_\varepsilon = \exp(-D_f \log(\varepsilon) + C_f), \varepsilon \in E^s\}. \quad (\text{B.2})$$

As a result, the l_2 -inferring unit provides an extra reconstruction constraint (i.e., $\min(E^{\text{SR}}) = 1$), which improves the accuracy of super-resolution. In this way, the expansion form of l_t in Eq. (8) reads

$$l_t = \frac{1}{|E^{\text{SR}}| L_a L_\beta} \left(\sum_{i \in E^s} \left\| \exp(-D_f \log(i) + C_f) - N_i(\sigma(\hat{\mathbf{x}}^{\text{SR}})) \right\|_2^2 + \sum_{j \in E^{\text{LR}}} \left\| N_{jf_u}(\sigma(\mathbf{x}^{\text{LR}})) - N_j(\sigma(\hat{\mathbf{x}}^{\text{SR}})) \right\|_2^2 \right). \quad (\text{B.3})$$

Appendix C. Numerical implementation for generating fractal primitives

In Cases C1a – e, a set of mapping functions $\{\phi_i : \mathbb{R}^2 \rightarrow \mathbb{R}^2\}_{i=1}^n$ is defined by the Iterated Function System approach, which generates self-affine fractal primitives through iterative processes. The corresponding numerical coordinates I is denoted as

$$I_{q+1} = \bigcup_{i=1}^{N_{\text{IFS}}} \phi_i(I_q), \quad (\text{C.1})$$

where q denotes the steps of iteration, with the mapping function represented by

$$\phi_i(I_q) = L(\epsilon^{\text{IFS}} A_q(\theta_i) I_q + B_i), \quad q \in \mathbb{N}, \quad (\text{C.2})$$

where L is the dimensionality of snapshots and $L = 512$ is applied in this study; A_q represents a rotational transformation matrix relating to the angle θ_i between the vector connecting the primitives and the horizontal axis; B_i denotes the translational transforming matrix. For example, Koch curve has the parameters of $q = 9$, $N_{\text{IFS}} = 4$, $\epsilon^{\text{IFS}} = 1/3$, and $I_0 = [0 \ 0]^T$, where $\theta_1 = \theta_4 = 0$, $\theta_2 = 60^\circ$, and $\theta_3 = -60^\circ$.

For two-dimensional fractal snapshots considered in this study (with dimensions $L \times L$), Eq. (C.2) can be expressed as

$$\phi_i \left(\underbrace{\begin{bmatrix} I_q^x \\ I_q^y \end{bmatrix}}_{I_q} \right) = L \bigcup_{i=1}^{N_{\text{IFS}}} \left(\epsilon^{\text{IFS}} \underbrace{\begin{bmatrix} \cos(\theta_i) & -\sin(\theta_i) \\ \sin(\theta_i) & \cos(\theta_i) \end{bmatrix}}_{A_q(\theta_i)} \underbrace{\begin{bmatrix} I_q^x \\ I_q^y \end{bmatrix}}_{I_q} + \underbrace{\begin{bmatrix} B_i^x \\ B_i^y \end{bmatrix}}_{B_i} \right), \quad (\text{C.3})$$

where the superscripts indicate the matrix components in two directions, i.e., x and y . Table C.1 presents the parameters of the IFS that generates snapshots with certain fractal dimensions (C1a - e), where C1a is not an iterated fractal but has the fractal dimension of 1.

Table C.1

Parameters of the IFS that generates fractal primitives.

C1	a	b	c	d	e
q	1	9	9	9	6
N_{IFS}	1	4	5	8	8
ϵ^{IFS}	1	1/3	1/3	1/4	1/3
I_0	$[0 \ 0]^T$	$[0 \ 0]^T$	$[0 \ 0]^T$	$[0 \ 1/2]^T$	$[0 \ 1/2]^T$
θ_i	$\theta_1 = 45^\circ$	$\theta_1 = \theta_4 = 0^\circ$, $\theta_2 = 60^\circ$, $\theta_3 = -60^\circ$	$\theta_1 = \theta_3 = \theta_5 = 0^\circ$, $\theta_2 = 90^\circ$, $\theta_4 = -90^\circ$	$\theta_1 = \theta_3 = \theta_6 = \theta_8 = 0^\circ$, $\theta_2 = \theta_3 = 90^\circ$, $\theta_5 = \theta_6 = -90^\circ$	$\theta_1 = \theta_3 = \theta_5 = \theta_7 = 0^\circ$, $\theta_2 = \theta_8 = 90^\circ$, $\theta_4 = \theta_6 = -90^\circ$
B_i	$B_1 = [0 \ 1]^T$	$B_1 = 0$, $B_2 = [1/3 \ 0]^T$, $B_3 = [1/2 \ \sqrt{3}/6]^T$, $B_4 = [2/3 \ 0]^T$	$B_1 = 0$, $B_2 = [1/3 \ 0]^T$, $B_3 = [1/3 \ 1/3]^T$, $B_4 = [2/3 \ 1/3]^T$, $B_5 = [2/3 \ 0]^T$	$B_1 = 0$, $B_2 = [1/4 \ 0]^T$, $B_3 = [1/4 \ 1/4]^T$, $B_4 = [1/2 \ 1/4]^T$, $B_5 = [1/2 \ 0]^T$, $B_6 = [1/2 \ -1/4]^T$, $B_7 = [3/4 \ -1/4]^T$, $B_8 = [3/4 \ 0]^T$	$B_1 = 0$, $B_2 = [1/3 \ 0]^T$, $B_3 = [1/3 \ 1/3]^T$, $B_4 = [2/3 \ 1/3]^T$, $B_5 = [2/3 \ 0]^T$, $B_6 = [1/3 \ -1/3]^T$, $B_7 = [2/3 \ -1/3]^T$, $B_8 = [2/3 \ 0]^T$

Appendix D. Description of turbulence DNS data

The detailed flow parameters of Cases C2a and C2b are referred to Refs [70,71] and [72,73], respectively. In Case C2a, the studied domain is $8\pi h \times 2h$, corresponding to the longitudinal velocity u on a 2-dimensional slice at $z = 1.5\pi h$, where h is the half channel height. The streamwise velocity fields have been collected for constituting snapshots and the dimensionless velocity range is 0 - 1.35. The centerline velocity $U_c = 1.13$ and the friction velocity $u_\tau = 5.00 \times 10^{-2}$, and their corresponding Reynolds numbers are $Re_c = 2.26 \times 10^4$ and $Re_\tau = 9.99 \times 10^2$, respectively. The fully-developed turbulence in the period from 4.0 - 24.0 is analyzed; the domain considered is 256×64 , and the time step is $\Delta t = 0.13$. In Case C2b, the size of the slice is $2\pi \times 2\pi$ and the dimensionless velocity range is -3.10 - 2.62. The Taylor-scale Reynolds number $Re_\lambda = 433$ and the Taylor microscale $\lambda = 0.118$. The spatial domain is 256×256 , the time step $\Delta t = 0.04$ s, the time range of 2 - 8 s is studied.

References

- [1] S.L. Brunton, B.R. Noack, Closed-loop turbulence control: progress and challenges, *Appl. Mech. Rev.* 67 (2015).
- [2] G. He, G. Jin, Y. Yang, Space-time correlations and dynamic coupling in turbulent flows, *Annu. Rev. Fluid Mech.* 49 (2017) 51–70.
- [3] A.S. Monin, On the nature of turbulence, *Soviet Physics Uspekhi* 21 (1978) 429.
- [4] A.N. Kolmogorov, Dissipation of energy in the locally isotropic turbulence, *Proceedings: Math. Phys. Sci.* 434 (1991) 15–17.
- [5] M.N. Hasan, T.E. Greenwood, R.G. Parker, Y.L. Kong, P. Wang, Fractal patterns in the parameter space of a bistable duffing oscillator, *Phys. Rev. E* 108 (2023) L022201.
- [6] L.F. Richardson, Weather Prediction By Numerical Process, University Press, 1922.
- [7] G.K. Batchelor, The Theory of Homogeneous Turbulence, Cambridge university press, 1953.
- [8] K. Duraisamy, G. Iaccarino, H. Xiao, Turbulence modeling in the age of data, *Annu. Rev. Fluid Mech.* 51 (2019) 357–377.
- [9] Y. Tian, M. Woodward, M. Stepanov, C. Fryer, C. Hyett, D. Livescu, M. Chertkov, Lagrangian large eddy simulations via physics-informed machine learning, *PNAS* 120 (2023) e2213638120.
- [10] D. Xiao, P. Yang, F. Fang, J. Xiang, C.C. Pain, I.M. Navon, M. Chen, A non-intrusive reduced-order model for compressible fluid and fractured solid coupling and its application to blasting, *J. Comput. Phys.* 330 (2017) 221–244.
- [11] X. Jia, C. Gong, W. Ji, C. Li, An accuracy-enhanced transonic flow prediction method fusing deep learning and a reduced-order model, *Phys. Fluids* 36 (2024).
- [12] S. Farsiu, D. Robinson, M. Elad, P. Milanfar, Advances and challenges in super-resolution, *Int. J. Imaging Syst. Technol.* 14 (2004) 47–57.
- [13] K. Nasrollahi, T.B. Moeslund, Super-resolution: a comprehensive survey, *Mach. Vision Appl.* 25 (2014) 1423–1468.
- [14] H. Kim, J. Kim, S. Won, C. Lee, Unsupervised deep learning for super-resolution reconstruction of turbulence, *J. Fluid Mech.* 910 (2021) A29.
- [15] Y. Sha, Y. Xu, G. Li, Y. Wei, C. Wang, Enhanced hydrofoil pressure field reconstruction through phase-informed sensing and sensor optimization, *Appl. Ocean Res.* 150 (2024) 104104.
- [16] Y. Xu, Y. Sha, C. Wang, Y. Wei, An improved deep learning model for sparse reconstruction of cavitation flow fields, *Phys. Fluids* 36 (2024).
- [17] P. Xie, R. Li, Y. Chen, B. Song, W.-L. Chen, D. Zhou, Y. Cao, A physics-informed deep learning model to reconstruct turbulent wake from random sparse data, *Phys. Fluids* 36 (2024).
- [18] H. Fan, S. Cheng, A.J. de Nazelle, R. Arcucci, ViTAE-SL: A vision transformer-based autoencoder and spatial interpolation learner for field reconstruction, *Comput. Phys. Commun.* 308 (2025) 109464.
- [19] J. Wu, D. Xiao, M. Luo, Deep-learning assisted reduced order model for high-dimensional flow prediction from sparse data, *Phys. Fluids* 35 (2023).
- [20] M. Raissi, Deep hidden physics models: deep learning of nonlinear partial differential equations, *J. Machine Learn. Res.* 19 (2018) 1–24.
- [21] K. Fukami, K. Fukagata, K. Taira, Super-resolution analysis via machine learning: a survey for fluid flows, *Theor. Comput. Fluid Dyn.* 37 (2023) 421–444.
- [22] K. Fukami, K. Fukagata, K. Taira, Super-resolution reconstruction of turbulent flows with machine learning, *J. Fluid Mech.* 870 (2019) 106–120.
- [23] K. Fukami, R. Maulik, N. Ramachandra, K. Fukagata, K. Taira, Global field reconstruction from sparse sensors with Voronoi tessellation-assisted deep learning, *Nat. Mach. Intell.* 3 (2021) 945–951.
- [24] Y. Lecun, Y. Bengio, G. Hinton, Deep learning, *Nature* 521 (2015) 436–444.
- [25] S. Li, J. Yang, P. Teng, Data-driven prediction of cylinder-induced unsteady wake flow, *Appl. Ocean Res.* 150 (2024) 104114.
- [26] X. Jin, S. Laima, W.-L. Chen, H. Li, Time-resolved reconstruction of flow field around a circular cylinder by recurrent neural networks based on non-time-resolved particle image velocimetry measurements, *Exp. Fluids* 61 (2020) 1–23.
- [27] A. Güemes, C. Sammiguel Vila, S. Discetti, Super-resolution generative adversarial networks of randomly-seeded fields, *Nat. Mach. Intell.* 4 (2022) 1165–1173.
- [28] X. Bi, A. Liu, Y. Fan, C. Yu, Z. Zhang, FlowSRNet: A multi-scale integration network for super-resolution reconstruction of fluid flows, *Phys. Fluids* 34 (2022).
- [29] J.S. Choi, E.S. Kim, J.H. Seong, Deep learning-based spatial refinement method for robust high-resolution PIV analysis, *Exp. Fluids* 64 (2023) 45.
- [30] H. Gao, L. Sun, J.-X. Wang, Super-resolution and denoising of fluid flow using physics-informed convolutional neural networks without high-resolution labels, *Phys. Fluids* 33 (2021).
- [31] K. Fukami, R. Maulik, N. Ramachandra, K. Fukagata, K. Taira, Global field reconstruction from sparse sensors with Voronoi tessellation-assisted deep learning, *Nat. Mach. Intell.* 3 (2021) 945–951.
- [32] K. Hornik, M. Stinchcombe, H. White, Universal approximation of an unknown mapping and its derivatives using multilayer feedforward networks, *Neural Networks* 3 (1990) 551–560.
- [33] H. Zhou, S. Cheng, R. Arcucci, Multi-fidelity physics constrained neural networks for dynamical systems, *Comput. Methods Appl. Mech. Eng.* 420 (2024) 116758.
- [34] H. Levine, Y. Tu, Machine learning meets physics: a two-way street, *PNAS* 121 (2024) e2403580121.
- [35] M.W. Berry, A. Mohamed, B.W. Yap, Supervised and Unsupervised Learning For Data Science, Springer, 2019.
- [36] G. Carleo, I. Cirac, K. Cranmer, L. Daudet, M. Schuld, N. Tishby, L. Vogt-Maranto, L. Zdeborová, Machine learning and the physical sciences, *Rev. Mod. Phys.* 91 (2019) 045002.
- [37] I. Goodfellow, J. Pouget-Abadie, M. Mirza, B. Xu, D. Warde-Farley, S. Ozair, A. Courville, Y. Bengio, Generative adversarial networks, *Commun. ACM* 63 (2020) 139–144.
- [38] M.Z. Yousif, L. Yu, H.-C. Lim, High-fidelity reconstruction of turbulent flow from spatially limited data using enhanced super-resolution generative adversarial network, *Phys. Fluids* 33 (2021).

- [39] T. Li, M. Buzzicotti, L. Biferale, F. Bonacorso, S. Chen, M. Wan, Multi-scale reconstruction of turbulent rotating flows with proper orthogonal decomposition and generative adversarial networks, *J. Fluid Mech.* 971 (2023) A3.
- [40] Z. Deng, C. He, Y. Liu, K.C. Kim, Super-resolution reconstruction of turbulent velocity fields using a generative adversarial network-based artificial intelligence framework, *Phys. Fluids* 31 (2019).
- [41] L. Nista, H. Pitsch, C.D. Schumann, M. Bode, T. Grenga, J.F. MacArt, A. Attili, Influence of adversarial training on super-resolution turbulence reconstruction, *Phys. Rev. Fluids* 9 (2024) 064601.
- [42] J. Fu, D. Xiao, R. Fu, C. Li, C. Zhu, R. Arcucci, I.M. Navon, Physics-data combined machine learning for parametric reduced-order modelling of nonlinear dynamical systems in small-data regimes, *Comput. Methods Appl. Mech. Eng.* 404 (2023) 115771.
- [43] B. Mandelbrot, How long is the coast of Britain? Statistical self-similarity and fractional dimension, *Science* 156 (1967) 636–638.
- [44] B.B. Mandelbrot, B.B. Mandelbrot, *The Fractal Geometry of Nature*, WH freeman New York, 1982.
- [45] P.A. Burrough, Fractal dimensions of landscapes and other environmental data, *Nature* 294 (1981) 240–242.
- [46] J. Theiler, Estimating fractal dimension, *JOSA a* 7 (1990) 1055–1073.
- [47] K. Falconer, *Fractal geometry: Mathematical Foundations and Applications*, John Wiley & Sons, 2014.
- [48] I. Procaccia, Fractal structures in turbulence, *J. Stat. Phys.* 36 (1984) 649–663.
- [49] K. Sreenivasan, Fractals and multifractals in fluid turbulence, *Annu. Rev. Fluid Mech.* 23 (1991) 539–604.
- [50] T. Xu, I.D. Moore, J.C. Gallant, Fractals, fractal dimensions and landscapes—a review, *Geomorphology* 8 (1993) 245–262.
- [51] P. Constantin, C. Foias, O.P. Manley, R. Temam, Determining modes and fractal dimension of turbulent flows, *J. Fluid Mech.* 150 (1985) 427–440.
- [52] B.B. Mandelbrot, B.B. Mandelbrot, Intermittent turbulence in self-similar cascades: divergence of high moments and dimension of the carrier, *Multifractals and 1/f Noise: Wild Self-Affinity Phys. (1963–1976)* (1999) 317–357.
- [53] K. Nagata, Y. Sakai, T. Inaba, H. Suzuki, O. Terashima, H. Suzuki, Turbulence structure and turbulence kinetic energy transport in multiscale/fractal-generated turbulence, *Phys. Fluids* 25 (2013).
- [54] K. Sreenivasan, C. Meneveau, The fractal facets of turbulence, *J. Fluid Mech.* 173 (1986) 357–386.
- [55] J. Vassilicos, J.C.R. Hunt, Fractal dimensions and spectra of interfaces with application to turbulence, *Proc. R. Soc. London. Series A: Math. Phys. Sci.* 435 (1991) 505–534.
- [56] B. Mazzi, J.C. Vassilicos, Fractal-generated turbulence, *J. Fluid Mech.* 502 (2004) 65–87.
- [57] G. Lane-Serff, Investigation of the fractal structure of jets and plumes, *J. Fluid Mech.* 249 (1993) 521–534.
- [58] M. Raissi, P. Perdikaris, G.E. Karniadakis, Physics-informed neural networks: A deep learning framework for solving forward and inverse problems involving nonlinear partial differential equations, *J. Comput. Phys.* 378 (2019) 686–707.
- [59] J. Wu, M. Luo, D. Xiao, C.C. Pain, B.C. Khoo, Koopman dynamic-oriented deep learning for invariant subspace identification and full-state prediction of complex systems, *Comput. Methods Appl. Mech. Eng.* 429 (2024) 117071.
- [60] M. Morimoto, K. Fukami, K. Zhang, A.G. Nair, K. Fukagata, Convolutional neural networks for fluid flow analysis: toward effective metamodeling and low dimensionalization, *Theor. Comput. Fluid Dyn.* 35 (2021) 633–658.
- [61] O. Ronneberger, P. Fischer, T. Brox, U-net: convolutional networks for biomedical image segmentation, in: *Medical image computing and computer-assisted intervention—MICCAI 2015: 18th international conference, Munich, Germany, October 5–9, 2015, proceedings, part III* 18, Springer, 2015, pp. 234–241.
- [62] K. He, X. Zhang, S. Ren, J. Sun, Deep residual learning for image recognition, in: *Proceedings of the IEEE Conference on Computer Vision and Pattern Recognition*, 2016, pp. 770–778.
- [63] F. Ren, W. Liu, G. Wu, Feature reuse residual networks for insect pest recognition, *IEEE Access* 7 (2019) 122758–122768.
- [64] J. Fu, S. Cui, S. Cen, C. Li, Statistical characterization and reconstruction of heterogeneous microstructures using deep neural network, *Comput. Methods Appl. Mech. Eng.* 373 (2021) 1–40.
- [65] Z. Li, N. Kovachki, K. Azizzadenesheli, B. Liu, K. Bhattacharya, A. Stuart, A. Anandkumar, Fourier neural operator for parametric partial differential equations, 2020, arXiv preprint arXiv:2010.08895.
- [66] J. Li, Q. Du, C. Sun, An improved box-counting method for image fractal dimension estimation, *Pattern Recognit* 42 (2009) 2460–2469.
- [67] G.-B. So, H.-R. So, G.-G. Jin, Enhancement of the box-counting algorithm for fractal dimension estimation, *Pattern Recognit. Lett.* 98 (2017) 53–58.
- [68] C. Panigrahy, A. Seal, N.K. Mahato, D. Bhattacharjee, Differential box counting methods for estimating fractal dimension of gray-scale images: a survey, *Chaos, Solitons Fractals* 126 (2019) 178–202.
- [69] H. Hentschel, I. Procaccia, Fractal nature of turbulence as manifested in turbulent diffusion, *Physical Review A* 27 (1983) 1266.
- [70] J. Kim, P. Moin, R. Moser, Turbulence statistics in fully developed channel flow at low reynolds number, *J. Fluid Mech.* 177 (1987) 133–166.
- [71] M. Lee, N. Malaya, R.D. Moser, Petascale direct numerical simulation of turbulent channel flow on up to 786k cores, in: *Proceedings of the International Conference on High Performance Computing, Networking, Storage and Analysis*, 2013, pp. 1–11.
- [72] G. Patterson, S.A. Orszag, Spectral calculations of isotropic turbulence: efficient removal of aliasing interactions, *Phys. Fluids* 14 (1971) 2538.
- [73] N. Cao, S. Chen, G.D. Doolen, Statistics and structures of pressure in isotropic turbulence, *Phys. Fluids* 11 (1999) 2235–2250.